Received: 19 April 2022 | Accepted: 7 October 2022

DOI: 10.1111/1752-1688.13080

AMERICAN WATER RESOURCES ASSOCIATION JAWRA JOURNAL OF THE AMERICAN WATER RESOURCES ASSOCIATION

RESEARCH ARTICLE

Diffusive wave models for operational forecasting of channel routing at continental scale

Md Nazmul Azim Beg[1] | Ehab A. Meselhe[1] | Dong Ha Kim[2,3] | James Halgren[4,5] | Adam Wlostowski[5,6] | Fred L. Ogden[3] | Trey Flowers[3]

[1]River-Coastal Science and Engineering, Tulane University, New Orleans, Louisiana, USA

[2]Remote Sensing Center, University of Alabama, Tuscaloosa, Alabama, USA

[3]NOAA/NWS Office of Water Prediction, National Water Center, Tuscaloosa, Alabama, USA

[4]Alabama Water Institute, University of Alabama, Tuscaloosa, Alabama, USA

[5]Lynker Technologies, Leesburg, Virginia, USA

[6]Boston Consulting Group, Boston, Massachusetts, USA

Correspondence
Md Nazmul Azim Beg, River-Coastal Science and Engineering, Tulane University, New Orleans, Louisiana, USA.
Email: mbeg@tulane.edu)

Funding information
NOAA Joint Technology Transfer Initiative (JTTI), Grant/Award Number: NA18OAR4590394

Abstract

Operational forecast models require robust, computationally efficient, and reliable algorithms. We desire accurate forecasts within the limits of the uncertainties in channel geometry and roughness because the output from these algorithms leads to flood warnings and a variety of water management decisions. The current operational Water Model uses the Muskingum-Cunge method, which does not account for key hydraulic conditions such as flow hysteresis and backwater effects, limiting its ability in situations with pronounced backwater effects. This situation most commonly occurs in low-gradient rivers, near confluences and channel constrictions, coastal regions where the combined actions of tides, storm surges, and wind can cause adverse flow. These situations necessitate a more rigorous flow routing approach such as dynamic or diffusive wave approximation to simulate flow hydraulics accurately. Avoiding the dynamic wave routing due to its extreme computational cost, this work presents two diffusive wave approaches to simulate flow routing in a complex river network. This study reports a comparison of two different diffusive wave models that both use a finite difference solution solved using an implicit Crank–Nicolson (CN) scheme with second-order accuracy in both time and space. The first model applies the CN scheme over three spatial nodes and is referred to as Crank–Nicolson over Space (CNS). The second model uses the CN scheme over three temporal nodes and is referred to as Crank–Nicolson over Time (CNT). Both models can properly account for complex cross-section geometry and variable computational points spacing along the channel length. The models were tested in different watersheds representing a mixture of steep and flat topographies. Comparing model outputs against observations of discharges and water levels indicated that the models accurately predict the peak discharge, peak water level, and flooding duration. Both models are accurate and computationally stable over a broad range of hydraulic regimes. The CNS model is dependent on the Courant criteria, making it less computational efficient where short channel segments are present. The CNT model does not suffer from that constraint and is, thus, highly computationally efficient and could be more useful for operational forecast models.

KEYWORDS
channel routing, Crank–Nicolson scheme, diffusive wave, flood forecasting, National Water Model

Research Impact Statement

This study compares two diffusive wave models based on finite difference solutions and implicit Crank–Nicolson schemes. Both approaches are computationally efficient and useable for operational models.

1 | INTRODUCTION

Flood forecasting and flood awareness have continued evolving for the last few decades. Operational flood forecasting has gained importance in the modern era due to the advancement of computational power and speed and has become an integrated part of improved disaster risk management (Beg et al., 2019; Carsell et al., 2004; Cloke & Pappenberger, 2009). Civil protection authorities get helpful decision-making information from the operational forecasts that are essential for saving lives and properties (Leandro et al., 2019; Meselhe et al., 2021). Early availability of flood warning information is a necessary key to reducing losses. However, the success of such forecasts depends significantly on the accuracy of river flow model prediction, which is related to initial state errors, forcing errors, and model structural errors (Madsen & Skotner, 2005).

The choice of flood routing may impact the predicted peak discharge, time of the peak discharge, depth, and extent of flooding (Alfieri et al., 2013; Meselhe et al., 1997; Mockus, 1967; Sabur & Steffler, 1996). There are several options to resolve the flow in one-dimensional (1D) or two-dimensional (2D) settings in a river flow prediction. While 2D modeling may provide more accurate and detailed information, the lack of high-resolution bathymetric and topographic data and associated high computational costs make the 1D hydrodynamic modeling approach the most viable option for large-scale operational flood forecasting (Barthélémy et al., 2018). For this modeling approach, the Saint-Venant equations proposed by Barre St. Venant (1871) remain the most comprehensive form of 1D flow description (Cunge, 1969; Ferrick, 1985; Ferrick et al., 1984). The Saint-Venant equations describe a set of two interdependent equations, known as mass conservation and momentum conservation equations. These equations are also known as the dynamic wave model in their full form and can simulate all types of flow regimes present in a river system (Fan & Li, 2006; Meselhe et al., 1997).

The dynamic wave model is superior in accuracy as long as all the hydraulic and channel geometry parameters are carefully defined (Ferrick, 2005; Litrico et al., 2010). Due to its numerical discretization, the model needs space–time data at sufficiently small intervals to represent real-world scenarios with minimal truncation errors. This makes dynamic models computationally demanding, requiring more careful input data verification to avoid instabilities (Meselhe et al., 2021). Some of the challenges encountered in an operational model implementation at the continental scale include the limited availability of bathymetric data. Furthermore, the heterogeneous nature of the hydraulic conditions at a large spatial scale results in numerical stability limits that necessitate a smaller time step to maintain the integrity of the numerical solutions (Ferrick et al., 1983). These issues often limit dynamic wave model usage in operational models.

Literature shows extensive effort finding appropriate simplified models for flow routing by simplifying or ignoring terms of the momentum conservation equation. These simplified hydraulics models are classified as diffusion or kinematic wave models. The diffusion wave assumes the inertia terms are negligible in the momentum conservation equation compared to the pressure, friction, and gravity terms. The kinematic wave further neglects pressure gradient terms compared to gravity terms. Some additional linear models are also developed by researchers, such as the Hayami model, Muskingum model, and stock model. These linear models have limitations, and are mostly acceptable only when the channel flow remains near the linearization point (Litrico et al., 2010).

The computational expense and possible numerical instabilities are challenging issues when running an operational forecast model like the National Water Model (NWM) (Cosgrove et al., 2021; Gochis et al., 2018). These issues become more concerning when considering the applicability of the dynamic model at such a large scale as the NWM covers the entire continental USA (Meselhe et al., 2021). The current update of the NWM (version 2.1) uses a simplified Muskingum-Cunge (MC) model (Cosgrove et al., 2021) built on a kinematic wave routing method with some refinements of the diffusive wave equation (Smith, 1980). The algorithm routes flow from the upstream end of a given channel, and progresses downstream in a cascading manner while considering no backwater effects (Brunner & Garbrecht, 1991). The model applies a storage relationship to the inflow–outflow calculation within a river reach (Chow et al., 1988) and involves a finite difference scheme to solve the river routing (Gochis et al., 2018). A thorough model evaluation showed favorable

agreement against field data (Brunner & Garbrecht, 1991). The MC model performance for computing discharge is comparable to the diffusive and dynamic wave approximations under certain conditions (Meselhe et al., 2021). However, the MC algorithm performs poorly for modeling low-gradient channels with backwater effects or strong tidal signals, with the most pronounced errors in modeled water levels (Meselhe et al., 2021).

The popularity of the diffusive wave model for unsteady flow routing in recent years stems from the fact that it often produces satisfactory solutions with reasonable accounting for downstream backwater effects (Fan & Li, 2006; Ferrick et al., 1984; Moussa & Bocquillon, 1996a; Wang et al., 2014). The diffusion wave routing requires less computational effort than the dynamic wave, making it more efficient for large network applications. As demonstrated later, the diffusive wave routing is more robust in the face of limited geometry data availability compared to dynamic wave routing. The assumption of neglecting inertial effects is valid for most of the slowly propagating flood waves, making the diffusive wave model viable for a broad range of hydraulic conditions (Cappelaere, 1997). In the diffusive wave method, the system of equations is reduced to a single parabolic equation using two parameters: celerity and diffusivity (Moussa, 1996). The equation can be solved analytically if these parameters (celerity and diffusivity) are considered constant (Cholet et al., 2017; Fan & Li, 2006; Hayami, 1951).

Given these advantages, we explored the applicability of certain formulations of the diffusive wave approximation in the context of operational hydraulic modeling. Specifically, we compared two diffusive wave models and tested their ability to hindcasting flood events at different hydraulic conditions. We applied a traditional Crank–Nicolson (CN) scheme in the first model and modified it to ingest input from non-uniform space grids using adapted Taylor's series and Hermite Interpolation method. We are referring to this method as Crank–Nicolson over Space or CNS. Alternatively, we examined an approach originally documented by Moussa and Bocquillon (1995, 1996b), which resolves the CN scheme over a uniform temporal spacing and then adapts the solution for the non-uniform spatial grid. The method is referred to as Crank–Nicolson over Time or CNT method. We modified both models to ingest inputs from natural cross-sections at highly non-uniform intervals, which is a prevalent issue when working with a continental-scale model. The ultimate objective of this effort is to examine the applicability of diffusive wave routing schemes for continental-scale operational forecast models.

2 | GOVERNING EQUATIONS

The St. Venant equations describing the 1D conservation of the fluid mass and momentum can be written as:

$$\begin{aligned} \frac{\partial A}{\partial t}+\frac{\partial Q}{\partial x}&=q_l \\ \frac{\partial Q}{\partial t}+\frac{\partial}{\partial x}\left(\frac{Q^2}{A}\right)+gA\frac{\partial h}{\partial x}&=gA\left(S_0-S_f\right), \end{aligned} \tag{1}$$

where Q is the discharge, A is the channel wetted area, t is the time, x is the distance, q_l is the lateral flow, h is the water depth, g is the gravitational acceleration, S_0 is the channel bed slope, and S_f is the friction slope.

In the case of diffusive model approximation, we neglect the two acceleration terms $\frac{\partial Q}{\partial t}$ and $\frac{\partial}{\partial x}\left(\frac{Q^2}{A}\right)$ from the momentum balance equation, and we can derive the following form of the diffusive wave equation by combining the two equations.

$$\frac{\partial Q}{\partial t}+C\frac{\partial Q}{\partial x}=D\frac{\partial^2 Q}{\partial x^2}+Cq_l, \tag{2}$$

where C and D are two additional parameters known as celerity and diffusivity, respectively, and are functions of channel flow, water depth, and geometry. A detailed derivation can be obtained from Cappelaere (1997) and Fan and Li (2006).

Equation (2) forms the governing equation of a typical diffusive wave, which we refer here as CNS diffusive wave.

Alternatively, we can assume C and D to be constant over time and space and then further partially differentiate Equation (2) with respect to x and t. Rearranging and ignoring the higher derivative terms, we arrive at the following equation (Moussa & Bocquillon, 1996b):

$$\frac{\partial Q}{\partial x}=\frac{-1}{C}\frac{\partial Q}{\partial t}+\frac{D}{C^3}\frac{\partial^2 Q}{\partial t^2}+\frac{2D}{C^4}\frac{\partial^3 Q}{\partial x\partial t^2}-\frac{D}{C^2}\frac{\partial q_l}{\partial t}+q_l. \tag{3}$$

Equation (3) forms the governing equation of the CNT diffusive wave.

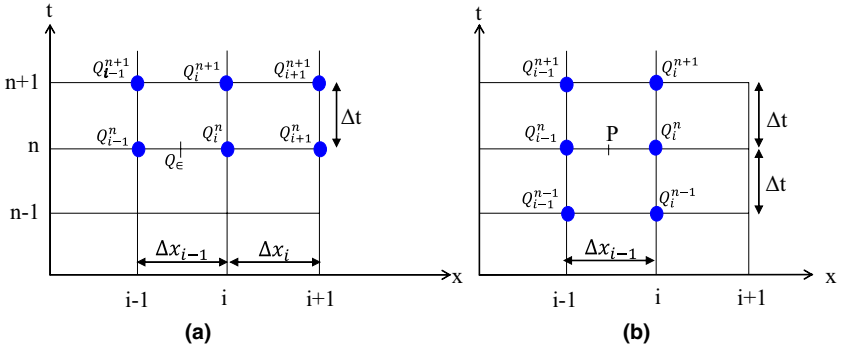

FIGURE 1 Space–time discretization of (a) Crank–Nicolson over Space (CNS) model and (b) Crank–Nicolson over Time (CNT) model.

3 | MODEL DISCRETIZATION

3.1 | CNS model

3.1.1 | Model formulation

We discretize the CNS model governing equation by numerically integrating the partial differential equation (Equation 2). A space–time discretization for the CNS method is sketched in Figure 1a. First, we consider:

$$\frac{dx}{dt} = C. \tag{4}$$

While ignoring lateral flow, the equation becomes,

$$\frac{\partial Q}{\partial t} = D\frac{\partial^2 Q}{\partial x^2}. \tag{5}$$

Then, we numerically integrating Equation (5) as follows:

$$Q_i^{n+1} = Q_\in + \int_{t_n}^{t_{n+1}} D\frac{\partial^2 Q}{\partial x^2} dt, \tag{6}$$

where Q_i^n is the discharge at value at ith space node and nth time node. $Q_\in$ is the phase of discharge between the nodes $i-1$ and i at time n, that can travel to the ith space node at $(n+1)$-th time. The total number of spatial computational node in the channel is denoted as nx.

Evaluating the integral in Equation (6) and assigning a time weighting θ to calculate the 2nd derivative, where $0 < \theta < 1$ results in the following equation:

$$Q_i^{n+1} = Q_\in + \Delta t D\left[(1-\theta)\frac{\partial^2 Q}{\partial x^2}\bigg|_{\epsilon_x} + \theta\frac{\partial^2 Q}{\partial x^2}\bigg|_i^{n+1}\right]. \tag{7}$$

A value of $\theta = 0.5$ converts Equation (7) to an integral based on trapezium rule.

At $\theta = 1$, the equation is fully implicit, and at $\theta = 0$ the equation is fully explicit. Using Taylor's series expansion, we can expand the term $\frac{\partial^2 Q}{\partial x^2}\big|_i^{n+1}$ as follows

$$\frac{\partial^2 Q}{\partial x^2}\bigg|_i^{n+1} = \frac{1}{\Delta x^2}\left[Q_{i+1}^n - (1+\alpha)Q_i^n + \alpha Q_{i-1}^n\right]\frac{2}{\alpha(1+\alpha)}, \tag{8}$$

where α is the ratio between two adjacent Δx's:

$$\alpha = \frac{\Delta x_i}{\Delta x_{i-1}}. \tag{9}$$

Rearranging Equation (7) leads to the following form:

$$Q_i^{n+1} = Q_\in + \Delta tD\left[(1-\theta)Q_{xx\in} + \frac{\theta}{\Delta x^2}\frac{2}{\alpha(1+\alpha)}\left\{Q_{i+1}^n - (1+\alpha)Q_i^n + \alpha Q_{i-1}^n\right\}\right], \tag{10}$$

where $Q_{xx\in}$ is the 2nd derivative of the flow phase $Q_\in$ between the points i and $i+1$.
Rearranging the terms further, we arrive at the following form:

$$Q_{i-1}^{n+1}\left(\frac{-\Delta tD\theta}{\Delta x^2}\frac{2\alpha}{\alpha(1+\alpha)}\right) + Q_i^{n+1}\left(1 + \frac{\Delta tD\theta}{\Delta x^2}\frac{2(1+\alpha)}{\alpha(1+\alpha)}\right) + Q_{i+1}^{n+1}\left(\frac{-\Delta tD\theta}{\Delta x^2}\frac{2\alpha}{\alpha(1+\alpha)}\right) = Q_\in + \Delta tD(1-\theta)Q_{xx\in}. \tag{11}$$

Equation (11) can be written as:

$$p_i Q_{i-1}^{n+1} + q_i Q_i^{n+1} + r_i Q_{i+1}^{n+1} = s_i, \tag{12}$$

where p_i, q_i, r_i, and s_i are coefficients that can be described as follows:

$$p_i = \left(\frac{-\Delta tD\theta}{\Delta x^2}\right)\frac{2}{\alpha(1+\alpha)}\alpha, \tag{13}$$

$$q_i = 1 + \frac{\Delta tD\theta}{\Delta x^2}\frac{2}{\alpha(1+\alpha)}(1+\alpha) = 1 - p_i\frac{(1+\alpha)}{\alpha}, \tag{14}$$

$$r_i = \left(\frac{-\Delta tD\theta}{\Delta x^2}\right)\frac{2}{\alpha(1+\alpha)} = p_i\frac{1}{\alpha}, \tag{15}$$

$$s_i = Q_\in + \Delta tD(1-\theta)Q_{xx\in}. \tag{16}$$

This set of equations includes $Q_\in$ and $Q_{xx\in}$. We can evaluate these values using two-point fourth-order Hermite interpolation between the discharge values and their first derivatives at the space nodes $i-1$ and i, such that:

$$Q_\in = a_1 Q_{i-1}^n + a_2 Q_i^n + a_3 Q_{xi-1}^n + a_4 Q_{xi}^n, \tag{17}$$

$$Q_{xx\in} = d_1 Q_{i-1}^n + d_2 Q_i^n + d_3 Q_{xi-1}^n + d_4 Q_{xi}^n, \tag{18}$$

where a_{1-4} and d_{1-4} are the coefficients of Hermite interpolation and Q_{xi}^n is the first-order differential of Q_i^n.

In these equations, Q_x^n appears as a dependent variable, for which values of $Q_\in$ and $Q_{xx\in}$ are subjected to advection. Considering the previous derivatives in Equation (10), we can arrive at the following expression:

$$Q_{xi}^{n+1} = Q_{x\in} + \Delta tD\left\{\theta\left(\frac{-\partial u}{\partial x}\right)_i^{n+1} Q_{xi}^{n+1} + (1-\theta)\left(\frac{-\partial u}{\partial x}\right)_\in Q_{x\in}\right\} + \Delta tD\left\{\theta\left.\frac{\partial^3 Q}{\partial x^3}\right|_i^{n+1} + (1-\theta)\left.\frac{\partial^3 Q}{\partial x^3}\right|_{\epsilon_x}\right\},$$

$$Q_{xi}^{n+1} = Q_{x\in} + \frac{\Delta tD\theta}{\Delta x^2}\left[Q_{xi+1}^n - (1+\alpha)Q_{xi}^n + \alpha Q Q_{xi-1}^n\right]\frac{2}{\alpha(1+\alpha)} + \Delta tD(1-\theta)Q_{xxx\in}, \tag{19}$$

where $Q_{x\in}$ and $Q_{xxx\in}$ are the first and third derivatives of the flow phase $Q_\in$, respectively.

Rearranging Equation (19) can lead to the following form:

$$Q_{x_{i-1}}^{n+1}\left(\frac{-\Delta tD\theta}{\Delta x^2}\right)\frac{2}{\alpha(1+\alpha)}\alpha + Q_{x_i}^{n+1}\left(1 + \frac{2\Delta tD\theta}{\Delta x^2}\frac{2}{\alpha(1+\alpha)}(1+\alpha)\right) + Q_{x_{i+1}}^{n+1}\left(\frac{-\Delta tD\theta}{\Delta x^2}\frac{2}{\alpha(1+\alpha)}\right) = Q_{x\in} + \Delta tD(1-\theta)Q_{xxx\in}. \tag{20}$$

This equation can be written as:

$$p_i Q_{x_{i-1}}^{n+1} + q_i Q_{x_i}^{n+1} + r_i Q_{x_{i+1}}^{n+1} = s_{xi}, \tag{21}$$

where,

$$s_{xi} = Q_{x\in} + \Delta tD(1-\theta)Q_{xxx\in}. \tag{22}$$

Equations (12 and 21) use the terms s_i and s_{xi}, respectively, as source terms for Q_i and Q_{xi}. The effect of lateral flow can be added, and Equation (16) is modified as follows:

$$s_i = Q_\in + \Delta t D(1-\theta)Q_{xx\in} + \Delta t C_i q_{li}. \tag{23}$$

The value of $Q_{x\in}$ and $Q_{xxx\in}$ can be evaluated from third derivative of cubic polynomial using Hermite interpolation:

$$Q_{x\in} = b_1 Q^n_{i-1} + b_2 Q^n_i + b_3 Q^n_{xi-1} + b_4 Q^n_{xi}, \tag{24}$$

$$Q_{xxx\in} = h_1 Q^n_{i-1} + h_2 Q^n_i + h_3 Q^n_{xi-1} + h_4 Q^n_{xi}, \tag{25}$$

where b_{1-4} and h_{1-4} are the coefficients of Hermite interpolation. The values of all the Hermite interpolation coefficients can be calculated as:

$$\begin{aligned} a_1 &= 3\mathrm{Cr}^2 - 2\mathrm{Cr}^3 \\ a_2 &= 1 - 3\mathrm{Cr}^2 + 2\mathrm{Cr}^3 \\ a_3 &= \left(\mathrm{Cr}^2 - \mathrm{Cr}^3\right)\Delta x_{i-1} \\ a_4 &= \left(-\mathrm{Cr} + 2\mathrm{Cr}^2 - \mathrm{Cr}^3\right)\Delta x_{i-1}, \end{aligned} \tag{26}$$

$$\begin{aligned} b_1 &= \left(6\mathrm{Cr} - 6\mathrm{Cr}^2\right)/\left(-\Delta x_{i-1}\right) \\ b_2 &= \left(-6\mathrm{Cr} + 2\mathrm{Cr}^2\right)/\left(-\Delta x_{i-1}\right) \\ b_3 &= \left(2\mathrm{Cr} - 3\mathrm{Cr}^2\right)(-1) \\ b_4 &= \left(-1 + 4\mathrm{Cr} - 3\mathrm{Cr}^2\right)(-1), \end{aligned} \tag{27}$$

$$\begin{aligned} d_1 &= \left(6 - 12\mathrm{Cr}^2\right)/\Delta x^2_{i-1} \\ d_2 &= \left(-6 + 12\mathrm{Cr}^2\right)/\Delta x^2_{i-1} \\ d_3 &= (2 - 6\mathrm{Cr})/\Delta x_{i-1} \\ d_4 &= (4 - 6\mathrm{Cr})/\Delta x_{i-1}, \end{aligned} \tag{28}$$

$$\begin{aligned} h_1 &= 12/\Delta x^3_{i-1} \\ h_2 &= -12/\Delta x^3_{i-1} \\ h_3 &= 6/\Delta x^2_{i-1} \\ h_4 &= 6/\Delta x^2_{i-1}, \end{aligned} \tag{29}$$

where:

$$\mathrm{Cr} = \frac{\Delta t}{\Delta x_{i-1}} C. \tag{30}$$

The system of Equations (17, 18, 24, and 25) can be rearranged as a system of linear equations as follows:

$$Q^{n+1}_i = E_i Q^{n+1}_{i=1} + F_i, \tag{31}$$

$$Q^{n+1}_{xi} = E_{xi} Q^{n+1}_{xi+1} + F_{xi}, \tag{32}$$

where:

$$E_i = \frac{-r_i}{p_i E_{i-1} + q_i}, \tag{33}$$

$$F_i = \frac{s_i - p_i F_{i-1}}{p_i E_{i-1} + q_i}, \tag{34}$$

$$E_{xi} = \frac{-r_i}{p_i E_{xi-1} + q_i}, \tag{35}$$

$$F_{xi} = \frac{s_{xi} - p_i F_{i-1}}{p_i E_{i-1} + q_i}. \tag{36}$$

3.1.2 | Boundary conditions

The set of Equations (31–36) represents a system of linear equations to calculate the Q_i^{n+1} along a given river reach. To solve this system of equations, external boundaries at both the upstream and downstream ends of a river reach are required. The upstream discharge boundaries are typically known from the hydrologic runoff calculations. If the downstream boundaries (tail water) are unknown, we used an additional node, also known as ghost node, to temporarily assign a downstream value. Ultimately, during a backward sweep (Meselhe et al., 1997), the downstream most location of a given channel network will be used to back-calculate water levels throughout the channel network. In this case, we consider the ghost node value Q_{nx+1}^{n+1}, at a distance of Δx_{nx-1} after the last node nx such that

$$Q_1^{n+1} = \text{coming from the boundary time series at the u / s}, \tag{37}$$

$$Q_{nx+1}^{n+1} = Q_{nx-1}^{n}. \tag{38}$$

3.2 | CNT model

3.2.1 | Model formulation

We discretize Equation (3) based on a central difference approach in time and forward differentiation in space. Figure 1b shows the space–time discretization for the CNT method. The equation considers equal spacing in time and non-uniform spacing in space. The partial derivatives can be written as:

$$\frac{\partial Q}{\partial x} = \frac{Q_i^n - Q_{i-1}^n}{\Delta x_{i-1}}, \tag{39}$$

$$\frac{\partial^2 Q}{\partial t^2} = \frac{1}{2}\left[\frac{Q_i^{n+1} - 2Q_i^n + Q_i^{n-1}}{\Delta t^2} + \frac{Q_{i-1}^{n+1} - 2Q_{i-1}^n + Q_{i-1}^{n-1}}{\Delta t^2}\right],$$

$$\frac{\partial^3 Q}{\partial x \partial t^2} = \frac{1}{\Delta x_{i-1}}\left[\frac{Q_i^{n+1} - 2Q_i^n + Q_i^{n-1}}{\Delta t^2} - \frac{Q_{i-1}^{n+1} - 2Q_{i-1}^n + Q_{i-1}^{n-1}}{\Delta t^2}\right].$$

Equation (3) can be rewritten as:

$$p_j Q_i^{n+1} + q_j Q_i^n + r_j Q_i^{n+1} = s_j'. \tag{40}$$

The right-hand side is known, and we consider:

$$s_j' = p_j' Q_{i-1}^{n-1} + q_j' Q_{i-1}^n + r_j' Q_{i-1}^{n+1} - \frac{D}{C^2}\frac{\partial q_l}{\partial t} + \Delta x q_l, \tag{41}$$

where p_j, q_j, r_j, p_j', q_j', and r_j' are functions of C, D, Δx, and Δt, such as

$$\begin{aligned} p_j &= \frac{-h}{4} - \frac{g}{2} - 2k \\ q_j &= 1 + g + 4k \\ r_j &= \frac{h}{4} - \frac{g}{2} - 2k, \end{aligned} \tag{42}$$

$$\begin{aligned} p_j' &= \frac{h}{4} + \frac{g}{2} - 2k \\ q_j' &= 1 - g + 4k \\ r_j' &= \frac{-h}{4} + \frac{g}{2} - 2k, \end{aligned} \tag{43}$$

$$\frac{\partial q_l}{\partial t} = \frac{q_{lj+1} - q_{lj-1}}{2\Delta t}, \tag{44}$$

and

$$\begin{aligned} h &= \frac{\Delta x}{C\Delta t} \\ g &= \frac{D\Delta x}{C^3\Delta t^2} \\ k &= \frac{D^2}{C^4\Delta t^2}. \end{aligned} \tag{45}$$

To solve this equation, we determine the coefficients E and F such that:

$$Q_i^n = E_j Q_i^{n+1} u_{j+1} + F_j, \tag{46}$$

and,

$$\begin{aligned} E_j &= \frac{-r_j}{p_j E_{j-1} + q_j} \\ F_j &= \frac{s_j' - p_j F_{j-1}}{p_j E_{j-1} + q_j}. \end{aligned} \tag{47}$$

We initialize $E_1 = 1$ and $F_1 = 0$.The space loop runs from $j = 2$ until $j = nt$ (last time step) and we calculate $E_{j=1,nt}$ and $F_{j=1,nt}$. Applying the value of Q_i^{n+1} (boundary condition), we can solve the system of linear equations.

3.2.2 | Boundary condition

The CNT model uses a central differentiation approach in time. The approach requires known boundary conditions at both ends of the time loop, that is., Q_i^1 and Q_i^{nt}, where nt is the last time step of the simulation. However, in a traditional hydraulic modeling approach, we know the flows $Q_1^{1:nt}$ as an upstream boundary and $Q_{1:nx}^1$ is generally known as the initial condition. The other required boundary condition $Q_{1:nx}^{nt}$ is generally unknown as it also depends on the simulation end time. In this work, we calculated the flows at the last time step boundary using a temporal ghost node at Q_i^{nt+1}, which is at $\Delta t_i'$ time interval after $t = nt$, as shown in Figure 2. For this approach, the values of p_j, q_j, r_j, p_j', q_j', r_j', and s_j' need recalculation for the non-uniform time grid settings at the boundary.

We can apply the following relationships (Equations 48 and 49) to Equations (42 and 43), and recalculate p_j, q_j, and r_j as shown in Equations (50 and 51)

$$\alpha_i = \frac{\Delta t_i'}{\Delta t}, \tag{48}$$

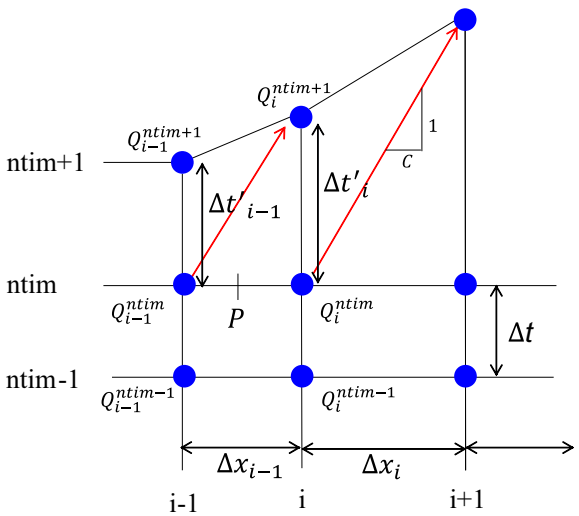

FIGURE 2 Discretization of CNT model boundary calculation.

$$\Delta t_i' = \frac{C}{\Delta x_{i-1}}, \tag{49}$$

$$\begin{aligned} p_j &= -\frac{1}{2(\alpha_i+1)}h - \frac{g}{2} - 2k \\ q_j &= 1 + \frac{\alpha_i+1}{2\alpha_i}g + \frac{2(\alpha_i+1)}{\alpha_i}k \\ r_j &= \frac{1}{2(\alpha_i+1)}h - \frac{1}{2\alpha_i}g - \frac{2}{\alpha_i}k, \end{aligned} \tag{50}$$

$$\begin{aligned} p_j' &= \frac{1}{2(\alpha_{i-1}+1)}h + \frac{g}{2} - 2k \\ q_j' &= 1 - \frac{\alpha_{i-1}+1}{2\alpha_{i-1}}g + \frac{2(\alpha_{i-1}+1)}{\alpha_{i-1}}k \\ r_j' &= -\frac{1}{2(\alpha_{i-1}+1)}h + \frac{1}{2\alpha_{i-1}}g - \frac{2}{\alpha_{i-1}}k, \end{aligned} \tag{51}$$

where,

$$Q_i^{nt+1} = Q_{i-1}^{nt+1} + \Delta x_{i-1} q_{lnt}. \tag{52}$$

After the model runs through all timesteps at the current spatial channel segment, it resolves the flow on the next (downstream) spatial segment. In this manner, the model computes all the spatial nodes and then updates the model parameters C and D using water depth data at the model downstream boundary. When restarting the model from a prior simulation, the model resolves the next timesteps using the updated C and D parameters. The values of E_{nt} and F_{nt} are also saved and used for the restart-simulation.

3.3 | Calculation of water level, celerity, and diffusivity

The calculation strategy for water level, celerity, and diffusivity is similar for both CNS and CNT methods. In a diffusive wave approximation, we neglect the effect of local acceleration $\frac{\partial Q}{\partial t}$ and convective acceleration $\frac{\partial}{\partial x}\left(\frac{Q^2}{A}\right)$ terms from the momentum conservation equation (Equation 1), and we hence reduce the momentum equation to

$$\frac{\partial h}{\partial x} = S_0 - S_f. \tag{53}$$

Discretizing Equation (53) in space, we obtain:

$$\frac{h_i - h_{i-1}}{\Delta x_i} = \frac{z_i - z_{i-1}}{\Delta x_i} - \frac{S_{f\,i-1} + S_{fi}}{2}, \tag{54}$$

where $S_{f\,i}$ is a function of Q_i, channel cross-section at i (A_i), and water depth at i (h_i). Using Manning's equation, we can estimate the friction slope $S_{f\,i}$ as follows:

$$S_{fi} = \frac{K_i^2}{Q_i^2}, \tag{55}$$

where K_i is the conveyance and is calculated as:

$$K_i = \frac{1}{n_i} A_i R_i^{\frac{2}{3}}, \tag{56}$$

where n_i is the Manning's coefficient and R_i is the hydraulic radius at the node i.

If the downstream boundary water level/depth (h_i) is known, then Equations (54–56) can be used in an iterative loop to obtain water level/depth at the immediate upstream node (h_{i-1}). For the approach presented here, we used Newton–Raphson formulation to obtain the water level at all the spatial nodes of the network.

Once the water level is known, we calculated the celerity and diffusivity using the following two equations following Litrico et al. (2010).

$$C_i = \frac{5S_{fi}^{0.3}Q_i^{0.4}}{3B(h)_i^{0.4}n_i^{0.6}}, \tag{57}$$

$$D_i = \frac{|Q_i|}{2S_{f_i}}\frac{1}{B(h)_i}, \tag{58}$$

where C_i and D_i are the celerity and the diffusivity at the node i. We algebraically averaged values of C_i and D_i over a river reach and calculated the values of C and D and used them in both, the CNS and CNT models.

$$C = \frac{1}{nx}\sum_{i=1}^{nx} C_i, \tag{59}$$

$$D = \frac{1}{nx}\sum_{i=1}^{nx} D_i. \tag{60}$$

3.4 | Junction boundary calculation

As presently formulated, both models handle a coalescing dendritic network only—there cannot be diverging junctions. At a junction node, if j numbers of channel reaches are connected, one river reach is defined as the downstream branch/collection branch. When calculating the discharge, the $j-1$ upstream reaches drain their discharge to the downstream reach. In the case of water level calculation, the water level at the upstream most node of the collection branch is applied to all the downstream nodes of the remaining $j-1$ upstream reaches.

3.5 | Limits on celerity and diffusivity

The calculation of celerity and diffusivity at different nodes (Equations 57 and 58) uses two empirical equations, and both have some limitations under certain conditions. In Equation (57), the presence of discharge in the numerator and the cross-section width in the denominator create computational challenges at low (or near-zero) flow conditions. For the test cases examined here, the cross-sections are approximated using compound trapezoidal sections, where the minimum section width remains equal to the bottom width. This is the current strategy used in the NWM. This approach creates a minimal value of celerity at near-zero discharge conditions. On the other hand, the presence of S_{f_i} in the denominator in Equation (58) creates a very large diffusivity value for low-gradient (or flat) sections of a given river. Such extreme cases are often encountered as the computations make dynamic adjustments according to their different hydraulic conditions. To accommodate these challenges, a set limits on the diffusivity and celerity values were used. These limits may introduce inaccuracies in the model, but they prevent spurious instabilities when these numerical conditions are inevitable.

Sensitivity analyses were performed to determine appropriate upper and lower limits that can be imposed on both the diffusivity and celerity to prevent numerical instabilities while minimizing the introduced error. We performed an array of tests applying different bounds of celerity (at an increment of 0.25 m/s) and diffusivity (at an increment of 50 m^2/s) and applied the conditions to different channels with varying bed slopes. Based on these test results, we adopted a lower and upper limit of diffusivity, 50 and 400 m^2/s, respectively, and a lower limit of celerity as 0.5 m/s. The tests also suggested an upper limit on the celerity, which we applied at three times the velocity at the cross-section, following Sriwongsitanon et al. (1998). Future tests may reveal further fine-tuning of these limits.

The CNT model has another stability criterion relating Δx, Δt, C, and D. Moussa and Bocquillon (1996b) described two dimensionless numbers Δx_+ and Δt_+ calculated as:

$$\Delta x_+ = \frac{C\Delta x}{D}, \tag{61}$$

$$\Delta t_+ = \frac{C^2\Delta t}{D}. \tag{62}$$

Very small values of Δx_+ and Δt_+ make the model unstable (Moussa & Bocquillon, 1996a, 1996b). Although the literature does not mention any lower limits of these values, sensitivity analysis by Moussa and Bocquillon (1996b) showed that the CNT model produces acceptable accuracy when

Δx_+ and Δt_+ stay between 0.1 and 0.5. For the CNT simulations in this work, we applied a more stringent minimum on the calculated D to provide a minimum Δx_+ of 0.1 and a minimum Δt_+ of 0.3.

4 | APPLICATIONS

4.1 | Single synthetic channel

We applied both the CNS and CNT models to a synthetic prismatic channel to test their performance. The channel has a longitudinal bed slope of 1:10,000 with a length of 20 km. The channel cross-sections are compound trapezoidal, as shown in Figure 3, resembling the channel geometry currently used in the NWM (Gochis et al., 2018). The cross-sections were spaced at a constant Δx of 1000 m. We applied a hypothetical discharge hydrograph at the upstream with a base flow of 20 m^3/s which increasing linearly to 25 m^3/s in 1 h then dropping to 20 m^3/s in 1 h (Figure 4). The downstream water depth is fixed at 4 m.

Figure 4 shows the single channel simulation results using the CNS and CNT models. Both models show a similar flood hydrograph at the downstream end. The flood peak magnitude and arrival times are almost identical, except for a slightly more diffused flood hydrograph produced by the CNT compared to the CNS approach.

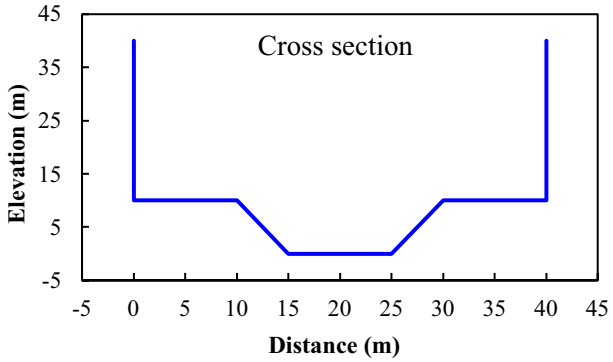

FIGURE 3 Cross-section of the single channel.

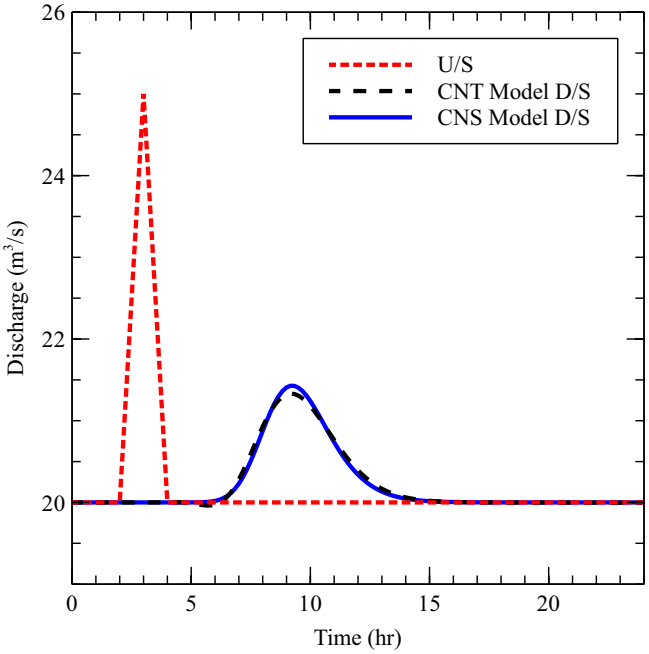

FIGURE 4 U/S and D/S discharge hygrograph from single channel test case.

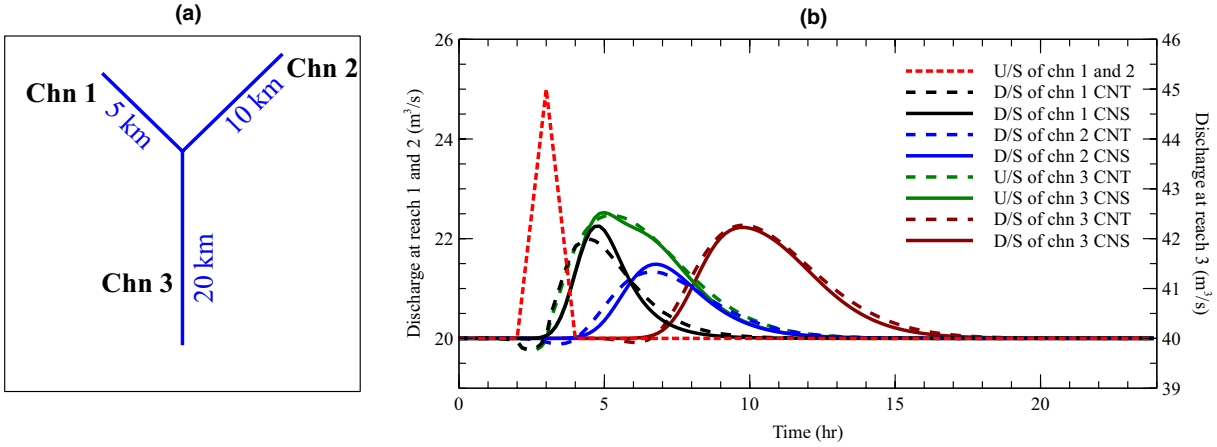

FIGURE 5 Simulation results from CNS and CNT model (b) at different computational points in a synthetic Y channel (a). The upper branches of the Y are designated channels 1 and 2 (Chn 1 and Chn 2), and the outflow below the junction is routed through channel 3 (Chn 3).

4.2 | Y-shaped synthetic network

We further tested the two models for a synthetic Y-shaped channel network. The three channels are 5, 10, and 20 km in length, respectively, and have the same cross-section shape, as shown in Figure 3. The domain has two u/s boundaries and one d/s boundary. We applied the same discharge and water levels boundaries as described in the previous test case.

From the simulation results of the Y-shaped network shown in Figure 5, we can see that the two models produce similar results. Like the single channel test case, the highest flood peak at the downstream was slightly more diffused in the CNT model than that of the CNS model. The two models downstream of channels 1 and 2 produced a slightly different flood hydrograph.

The mass balance of each model was checked. The mass balance error was 0.03% for CNS and 0.12% for the CNT model.

4.3 | Lower Mississippi River (Louisiana, USA)

The Lower Mississippi River reach considered here has an average discharge of 17,000 m^3/s. We applied the CNT and CNS models for the 2011 calendar year where a significant flood event was experienced. The model upstream boundary is located at Tarbert Landing (point 01 in Figure 6), Louisiana (USACE gage no 0100Q), and the downstream boundary was placed at the Head of Passes (point 16 in Figure 6), near the outfall of the Mississippi River to the Gulf of Mexico. This river reach is approximately 400 km in length. There are seven discharge extraction points within this reach length: the Bonnet Carré Spillway, Davis Pond, Caernarvon, Naomi, West Point a la Hache, Bohemia, and Fort St. Philip. These extractions were applied as lateral flow time-series data. While detailed cross-section data were available, we opted to use the simplified compound trapezoidal cross-sections used in the NWM to allow straightforward comparison to MC-based simulations. The spacing between the cross-sections varies between 183 m and 27.7 km. The upstream discharge and the downstream water level boundaries were taken from USGS and USACE stations (USACE Gage no 0100Q and 01515, respectively, can be accessed from https://rivergages.mvr.usace.army.mil/).

As shown in Figure 7, both the CNS and CNT models produced similar results. The discharges and water level hydrographs produced by both models agreed well with the measurements. It should be noted that the water levels shown in Figure 7 are in reference to the NAVD88 datum.

4.4 | Goodwin Creek (Mississippi, USA)

Goodwin creek is a small watershed located in the North-central part of Mississippi state. The catchment area has a steep topography (average channel slope is 0.4%) and a drainage area of 21.4 km^2 (Downer & Ogden, 2004; Ogden & Julien, 1993). The watershed elevation ranges from 71 m near the outlet to 128 m at the catchment edges. This humid climatic region has an average annual rainfall of 1440.2 mm, yielding an average runoff of 144.8 mm (Meselhe et al., 2009). Due to the smaller size of the catchment area and steep topography, the catchment experiences flashy flood peaks during rainfall events.

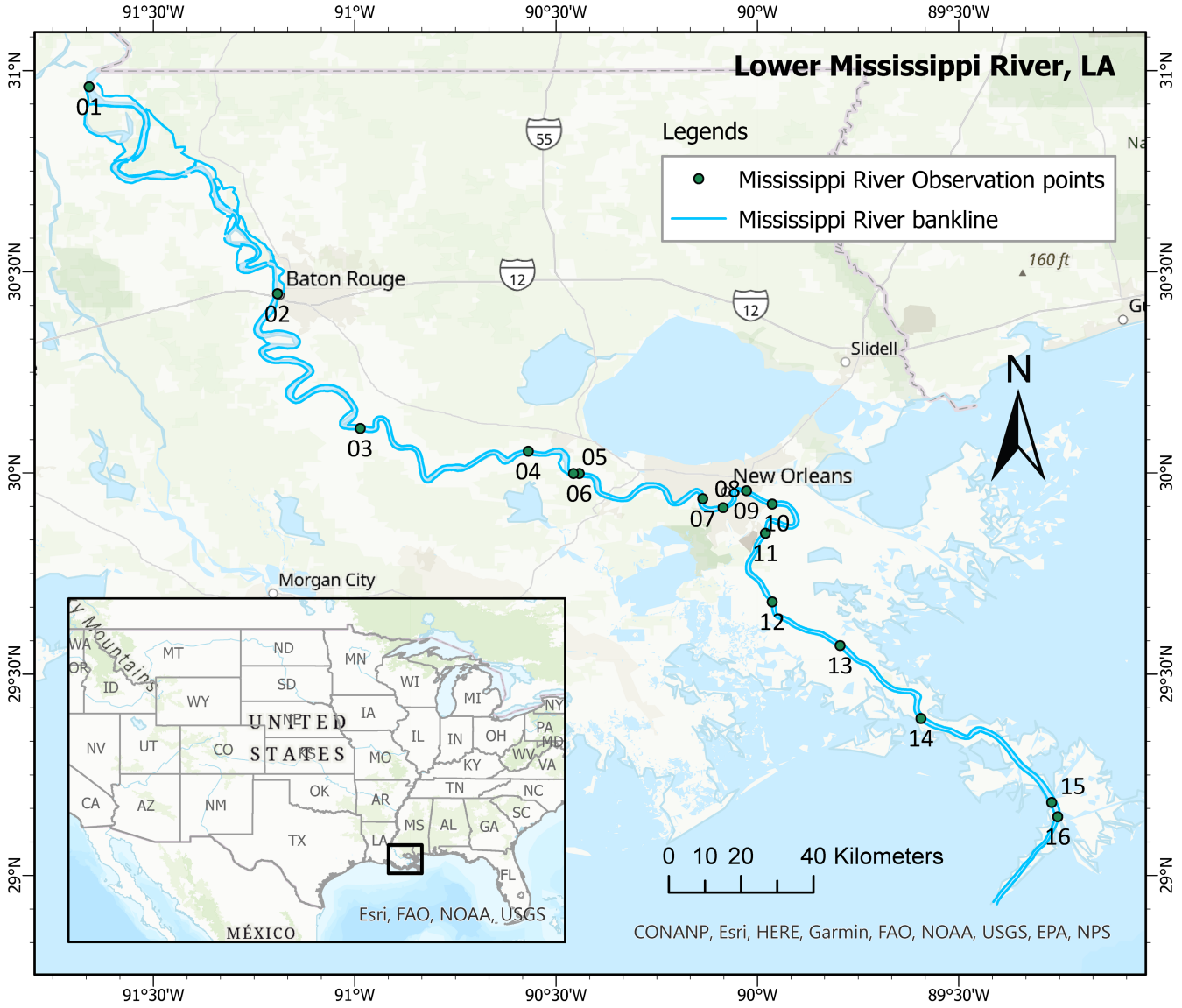

FIGURE 6 Map shows Lower Mississippi River area with all the observed data locations along the river reach. The index map at the bottom left indicates the extent of the river using a rectangle.

This creek serves as an experimental watershed under the United States Department of Agriculture (USDA) and has available historical data of rainfall, discharge, and water level from 1982 to 2002 (Ogden & Julien, 1993). The watershed had 30 rainfall stations and 10 locations with discharge and water depth measurements. Figure 8 shows the locations of the rainfall gages and stream measurement locations. We retained the same gage numbering as the original USDA project for clarity and future reference. Only the gage stations that had enough data for this event were used in this work. A pre-calibrated HEC-HMS model (Meselhe et al., 2009) utilized the rainfall data to produce the generated runoff results used as our model discharge inputs. The cross-section data were taken from the corresponding channel segments from the NWM database. The measured water depths at Gage 01 were used for downstream boundary conditions. We used a rainfall event from 1982 to test our model for this case.

Figure 9 compares the measured discharge and water depth at several locations. The figure indicates that the case exhibits kinetic wave behavior as the hydrographs indicate a sharp rise and a sharp fall within a short period and the sharp wave is preserved as it progresses downstream. Although the two diffusive wave models are mainly proposed to replicate backwater effects, they can also simulate kinematic wave phenomena. The comparison indicates that both the CNS and CNT results were in good agreement with the measurements. At the location of Gage 14, the modeled discharge and water levels were different than the observations but this mismatch is attributed to errors in the simulated hydrological responses in the upstream branches. No MC model data were available for this case to compare with the diffusive wave model results.

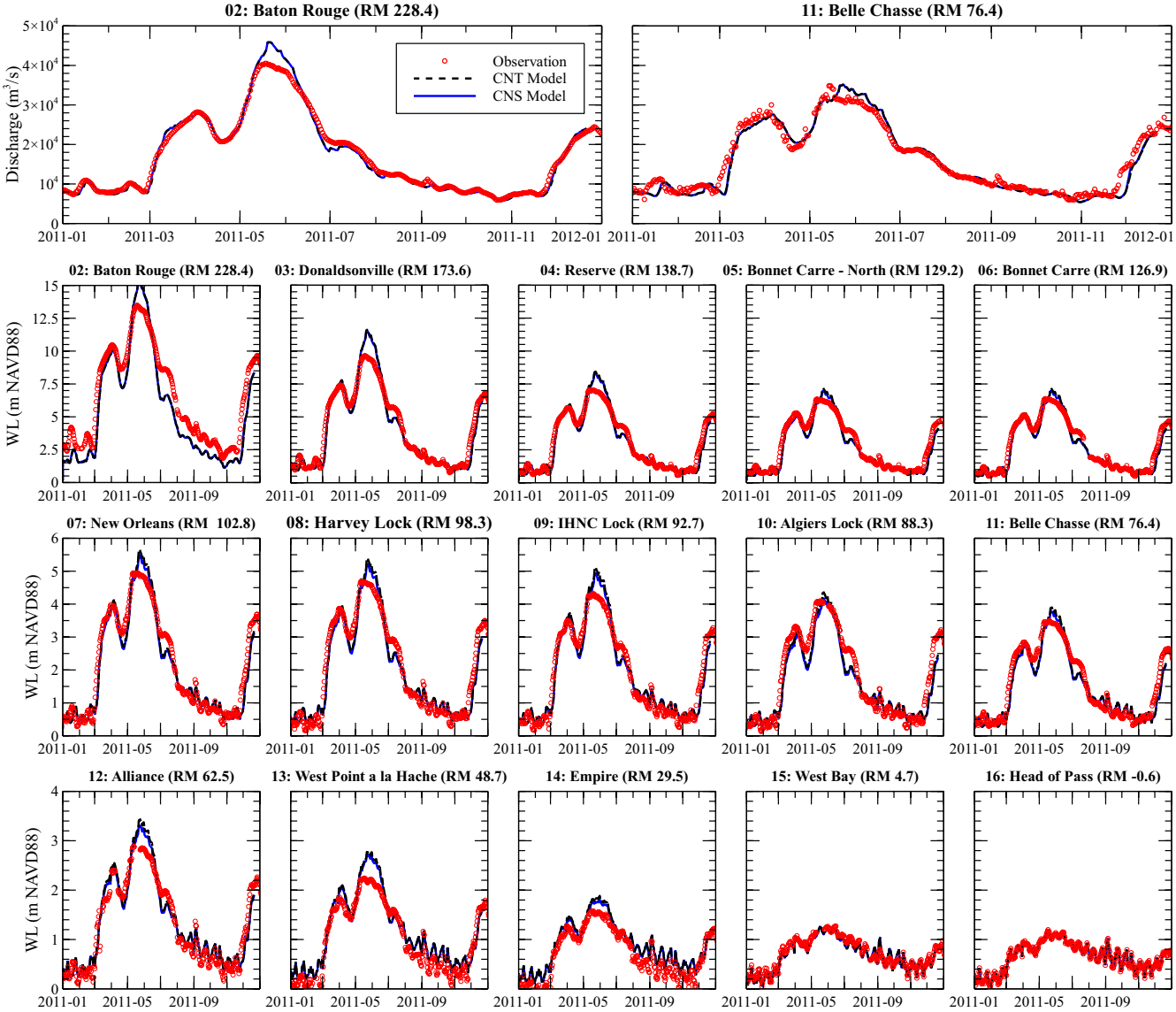

FIGURE 7 Comparison of discharge and water levels from Mississippi test cases. All water levels are in NAVD88 datum. The USACE designated River Milage (RM) values are indicated at each subtitle, measuring the distance of the station from the river mouth at the Gulf of Mexico. The numerical station numbers are indicative to the station locations in Figure 6.

4.5 | Amite-Comite River (South-East, Louisiana)

The Amite River starts from East Fork Amite River and West Fork Amite River in the Mississippi, USA, and confluences around 1.5 km south of Mississippi-Louisiana border (Figure 10). The river then flows to the south into Lake Maurepas in Louisiana, USA. At the city of Denham Springs, the river meets the Comite River approximately 90 km upstream of the outfall into Lake Maurepas, and the two rivers drain nearly 4880 sq. km of the total watershed area. The downstream part of the river has a wide and unconfined floodplain, which remains permanently at or near bank full.

For the analysis presented here, we focused on the flood event of August 2016 for the Amite-Comite River. This was classified as a 550-year return period event (van der Wiel et al., 2017). For the model setup, we again utilized the channel cross-section geometry used in the NWM dataset. Initial tests confirmed that the cross-section widths specified in the NWM channel database for the Amite-Comite rivers were severely underestimated the actual dimensions. As an alternative to the NWM channel geometry dataset, and guided by actual channel surveys, we adjusted the cross-sections by widening the represented floodplains for the lower part of the river. The diffusive model results from simulations performed on the adjusted sections were compared with data from five USGS monitoring stations (Figure 11). For comparison, we also included the MC model results. The MC model used the same setup as the two diffusive models. The model used runoff hydrographs produced by a

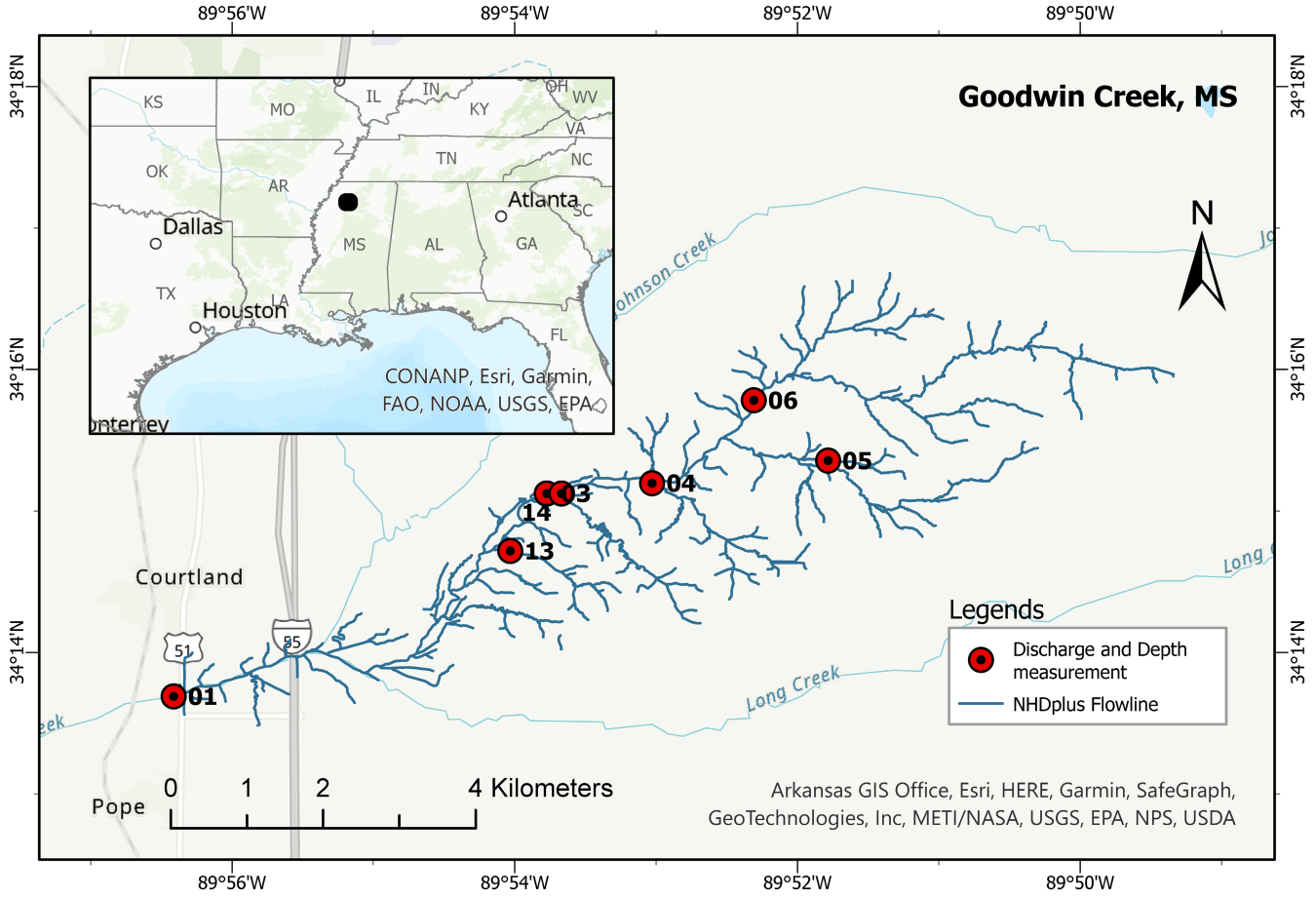

FIGURE 8 Goodwin creek catchment area with the measurement locations of discharge and water depth. The index map at the top left indicates the location of the creek using a black dot.

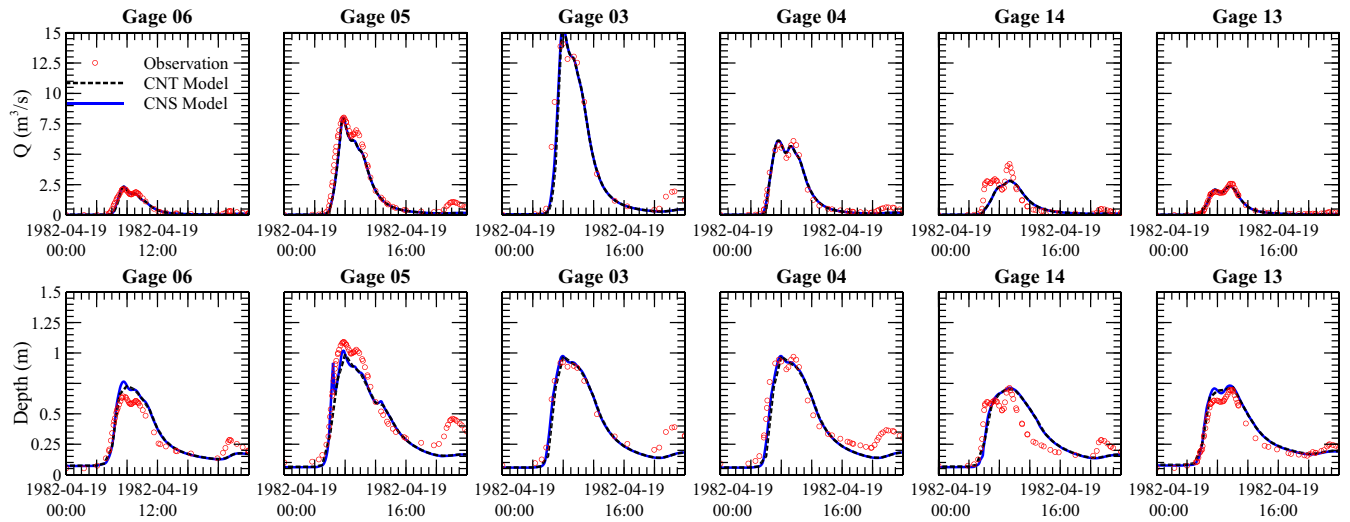

FIGURE 9 Comparison of discharge and water depths at different locations of Goodwin creek. The first row indicates the discharge comparison while the second row shows the water depth comparison at the same locations.

calibrated rainfall-runoff model (Dewberry Engineers Inc, 2019). Downstream boundary water levels were obtained from USGS water level observations at Lake Maurepas.

As shown in Figure 11, both diffusive models showed similar flood discharge peaks; however, they differed slightly from the MC outputs. At Gage 07380120, the CNS and the CNT models showed different phases in the flood waves. Overall, both diffusive wave models and the

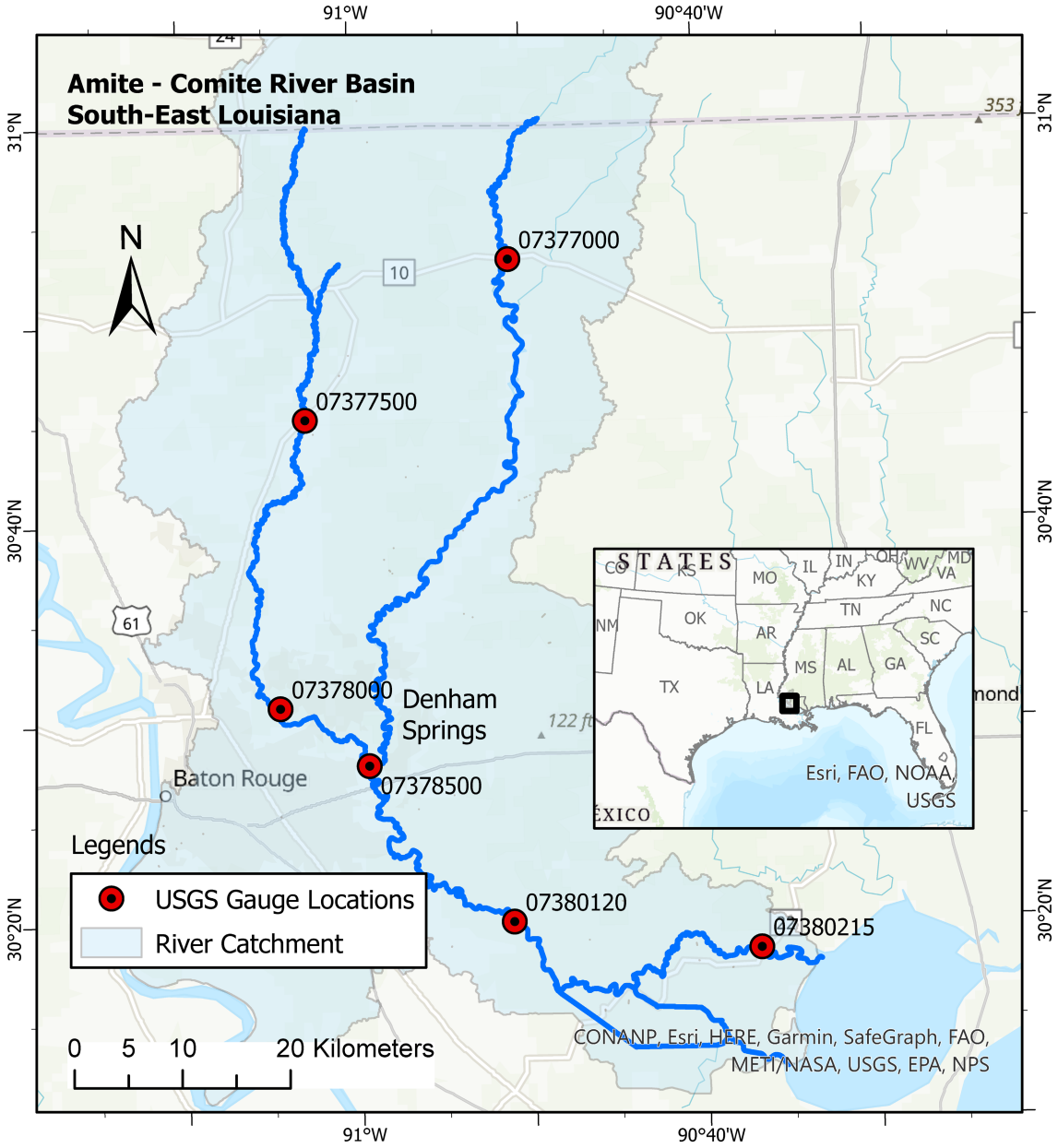

FIGURE 10 Map shows Amite-Comite River area with all the USGS observed data locations. The black rectangle indicates the extent of the river in the index map.

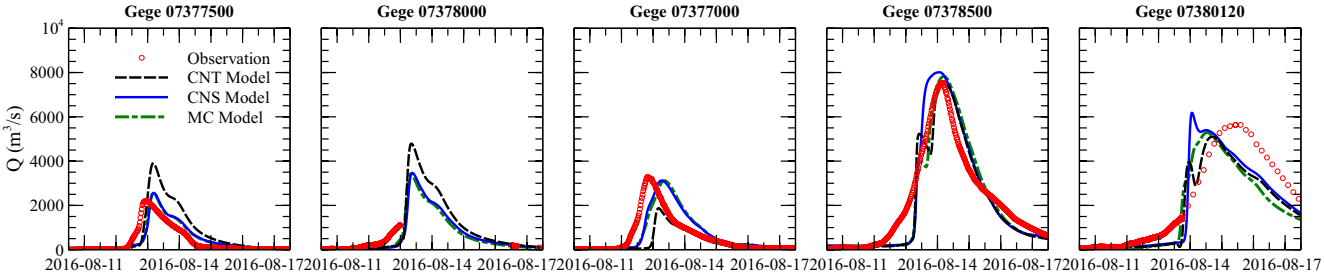

FIGURE 11 Comparison between discharge at the Amite-Comite River Basin.

MC model agreed well with the flow measurements. However, as the simplified geometry used here severely underestimated the flood plain capacity, the water level calculations were strongly influenced. Adjusting the cross-section geometry based on actual surveys allowed the diffusive wave models to produce reasonable water level hydrographs. The MC method did not produce good water level hydrographs even

for the adjusted geometry as it lacks the ability to capture any backwater effect. This issue is elaborated and discussed in a later section of the paper.

4.6 | Falls Lake (North Carolina, USA)

We applied the diffusive wave models to a river basin network in the state of North Carolina (Figure 12). The watershed in discussion is in the Neuse River basin located at upstream of Falls Lake. We incorporated a subset of the NWM river network containing 737 river reaches from a portion of the Neuse River basin. The spatial node to node distances (Δx) varied from 20 to 3000 m, with many of the upstream channels having only two spatial nodes in the river reach (only one Δx). The watershed is fairly flat, with a catchment area of approximately 1100 km^2.

We simulated the flood event following Hurricane Florence to test our models. This was a Category 4 major hurricane with a maximum sustained wind speed of 215 km/h (130 m/h). Intense precipitation created flooding in significant areas of North and South Carolina states. We collected the rainfall-runoff simulation results from the WRF-Hydro model and applied them as lateral inflow boundaries to the channels. The simulated network extended to the watershed boundaries, so there were no upstream headwaters. We also simulated an MC model for the watershed and compared the results with the diffusive models.

Figure 13 shows the comparison of discharge hydrographs produced by the CNS, CNT, and MC models at the available USGS stations within the watershed. For the discharge hydrographs, the CNT model produced comparable results to the MC, while the CNS overestimated the peak discharge at several locations. For the water level hydrographs, the CNS and CNT models were in reasonable agreement with the measurements while the MC model overestimated the peak water level, likely due to the use of normal depth assumptions which is not suitable for this watershed with flat terrain.

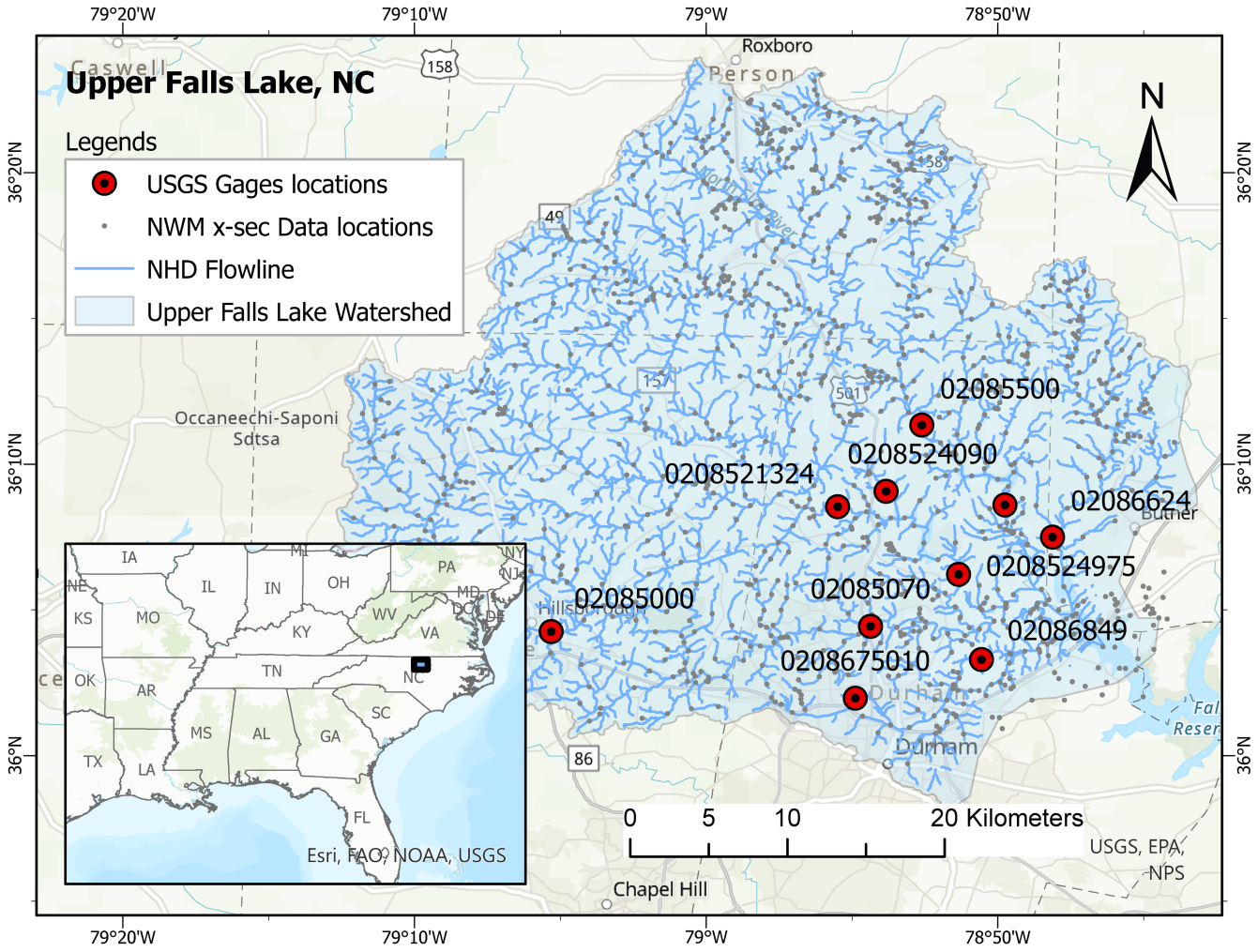

FIGURE 12 Map shows upper falls Lake catchment area with all the USGS observed data locations in the watershed. The index map at the bottom left indicates the extent of the river using a rectangle.

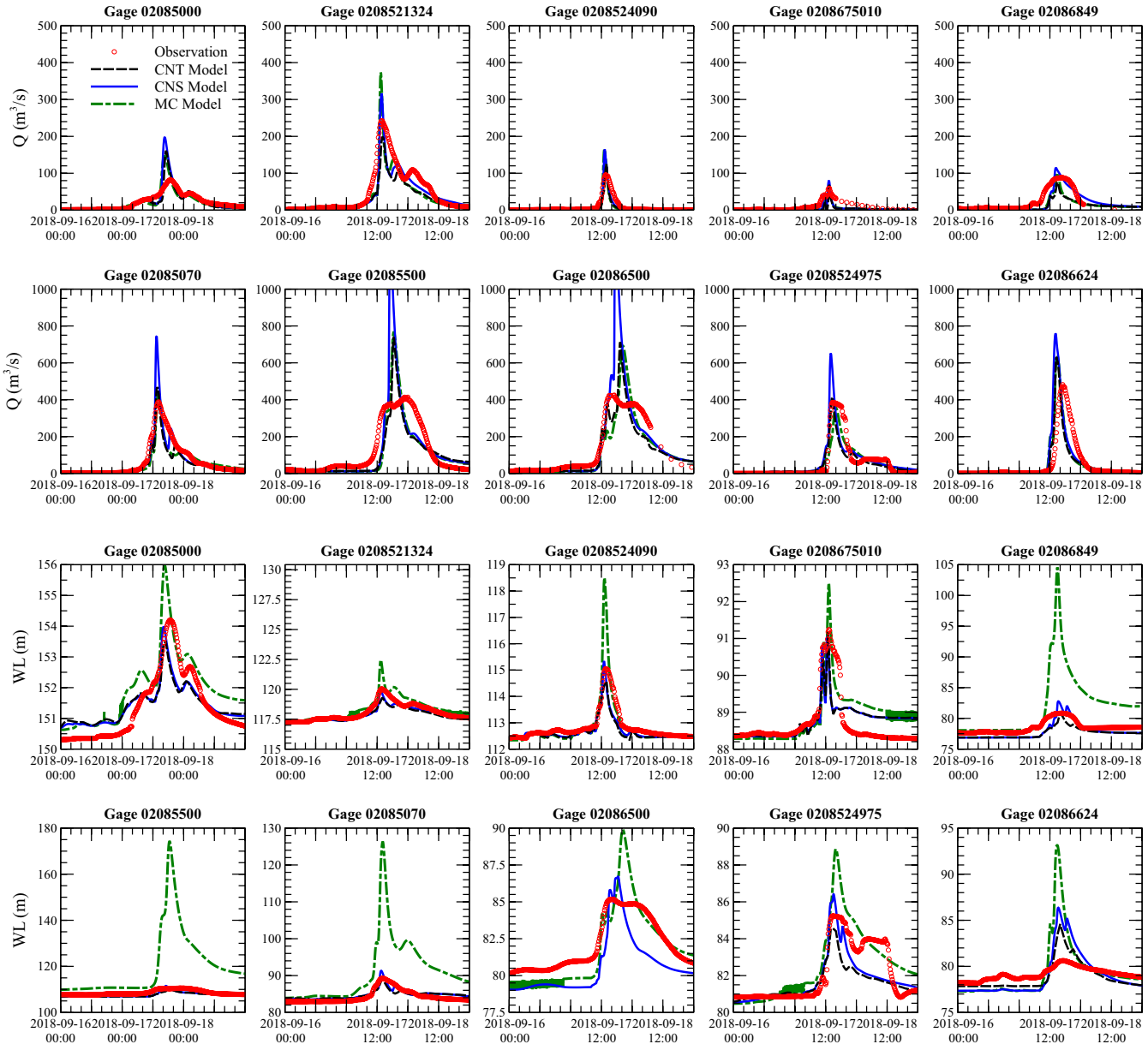

FIGURE 13 Discharge and water level compared to USGS station observations from the falls Lake test case. The top two rows provide the discharge comparison while the last two rows provide the water level comparison at the same stations.

5 | DISCUSSION

5.1 | Kinematic (MC) comparison to diffusive wave routing

The flow routing in the MC model is not influenced by the modeled water depths; rather, a normal depth is assumed throughout the model domain. On the other hand, the diffusive flow routing relies on the water depth to calculate the celerity and diffusivity parameters. The celerity and diffusivity are functions of the discharge, river geometry, and water depth. This makes the diffusive model sensitive to the proper application of the downstream water level boundary and accurate channel geometry data, whereas the MC flow routing is largely independent of the channel cross-section geometry.

For example, in the application of Amite-Comite River, the river cross-sections in the NWM database do not capture the proper floodplain capacity, which resulted in unreasonably large water depths. The water depth calculated by the diffusive wave models improved significantly when the surveyed floodplain geometry is used. Interestingly, the flow hydrographs calculated by the MC model were not changed by the different versions of the geometry. In most cases, the modeled peak discharge, time of peak flow, and total water flow volume from the MC model were very close to the observed data, regardless of errors in the modeled depth. This confirms the disconnection between the MC

routing method and the local water depth calculations. As expected, and due to the coupling between the flow and water depth calculations, the flow routing for both diffusive models was directly affected by the quality of the geometry data.

When the channel geometry is properly represented, the diffusive flood routing is expected to capture the backwater effects and the proper time of arrival of the flood peaks. It is anticipated as the quality of the National Hydrographic Database (NHD) geometry improves, a diffusive wave routing model would produce a higher quality forecast for flood depths, duration, and the peak time of arrivals.

The MC and diffusive wave models can perform equally well for steep gradient regions (i.e., headwaters) where the water depth is relatively uniform (and close to normal depth), and backwater effects are rare. This phenomenon is seen in the Falls Lake test case in Figure 13, where the USGS Gage 08085500, 028524090, and 028675010 are located at the upper part of the Neuse River basin. At these locations, the MC and CNT models provided comparable results. Gage 0208524975 is located further downstream, where the CNT model showed better agreement with the field observations compared to the MC approach.

Overall, both diffusive models produced reasonable water depth predictions compared to the field observations.

5.2 | Bathymetric data availability

The NWM channel network database includes channel cross-sectional data at 2.7 million river locations across the contributing drainage areas of the Continental U.S. (CONUS). The database contains the river reaches based primarily on the segmentation of the NHD Plus dataset. The channel geometry is represented through a simplified compound trapezoidal section derived from terrain analyses (Gochis et al., 2018). The geometry approximation at times may not accurately represent the true channel or floodplain capacities. For example, in the case study of the Amite-Comite River, we compared the available NWM cross-sections with actual surveys at the same locations. The comparison illustrates that the NWM cross-section matches main-channel capacity reasonably well, but largely underestimates the floodplain capacity (Figure 14).

Furthermore, the cross-section data are processed such that no adverse slope is allowed in the database as the MC method does not allow for zero or adverse channel slopes. This alteration results in inconsistencies in the overall longitudinal slope of the channel network and affects the wave propagation (time of travel and attenuation), which affects the simulation of backwater and other dynamic hydraulic effects.

While the MC method is not significantly affected by the quality of the channel geometry, the diffusive wave methods would certainly benefit from future improvements to the NHD. As noted in the model results comparison in Figure 11, the current results of the diffusive wave models did not capture the backwater effect properly as compared to the observed data. While the 8-point compound trapezoidal section was used for these simulations to facilitate comparison with MC model results, the two diffusive wave models applied in this study can directly accommodate complex surveyed cross-sections and are not limited to a more simplified channel geometry description. As the NWM cross-section database improves in the future updates considering the ability to capture the channel and floodplain capacity, the quality of the depth and discharge hydrographs produced by the diffusive wave methods will also improve.

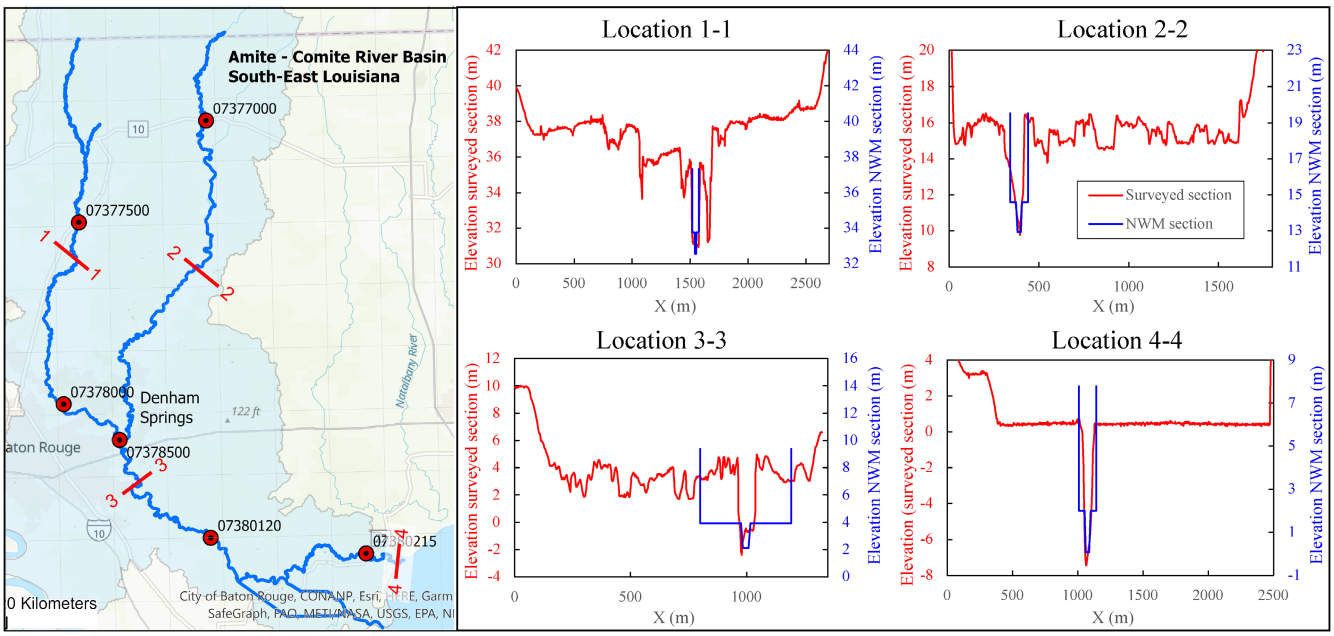

FIGURE 14 Comparison of National Water Model database cross-sections with surveyed sections.

5.3 | Differences between CNS and CNT models

Although both CNS and CNT models start from the same diffusive wave assumption, that is, ignoring the acceleration terms from the St. Venant equations, they exhibit differing numerical stability limits that ultimately influence their computational efficiency. Specifically, in the CNT method, and as described earlier, we further partially differentiate the CNS governing equation (Equation 2) and ignore some higher-order terms such as $\frac{\partial^4 Q}{\partial x^3 \partial t}$ and $\frac{\partial^4 Q}{\partial x^4}$ (Moussa & Bocquillon, 1996b). While CNS might be superior in accuracy as the governing equation contains more terms (Moussa, 1996; Moussa & Bocquillon, 1995, 1996a), the CNT method is more flexible for practical implementations (e.g., variable spatial spacing) and more computationally efficient. Given the extreme disparity in riverine segment lengths in the NWM dataset (varying from few meters to several kilometers) dictate the utility of small time steps to accommodate the stability limitation of the CNS model. Such limitation does not exist for the CNT model.

The two models apply the diffusive wave equation differently. For the CNS method, the calculation remains within one temporal layer of the space–time continuum and solves all the variables at all the spatial locations at the same temporal level. The model can be extended spatially before solving any variable at the next temporal level. However, in the CNT model, the model needs to solve all the temporal variables at a certain spatial location before it proceeds to the next river segment. Due to this fundamental difference, as the role of the time and space axis are interchanged, these models require specific treatment for their boundary condition setup. The CNS requires boundary values at $Q^{1}_{1:nx}$, $Q^{1:nt}_{1}$ and $Q^{1:nt}_{nx}$ while the CNT requires boundary conditions at $Q^{1}_{1:nx}$, $Q^{1:nt}_{1}$, and $Q^{nt}_{1:nx}$. These numerical differences may create slightly different results between the two models even if the celerity and diffusivity parameters are assigned similar values (Moussa & Bocquillon, 1996b).

Due to the differences in discretization, the CNS model cannot accurately accommodate true distributed lateral flow inputs. Rather, the flow is accumulated as a series of point-sources imposed at the upstream edge of a channel segment, leading to inaccuracy of the flood-peak timing (i.e., phase error). On the other hand, the lateral flow in the CNT method is incorporated uniformly along the length of the channel.

TABLE 1 Comparison of statistical model performance between modeled and observed flow for each of the two models for the simulated events.

		CNS		CNT		Peak discharge (m^3/s)
Case study	Station name	BIAS (m^3/s)	RMSE (m^3/s)	BIAS (m^3/s)	RMSE (m^3/s)	
Lower Mississippi 2011-01-01–2011-12-31 (365 days)	Baton Rouge	17.16	1370.74	60.295	1407.52	40,210
	Belle Chasse	369.73	1919.64	397.442	1986.89	34,830
Goodwin Creek 1982-04-19 (24 h)	Gage 06	0.03	0.22	0.00	0.24	2.2
	Gage 05	−0.20	0.97	−0.23	0.99	8.0
	Gage 03	−0.08	1.39	−0.38	1.89	14.0
	Gage 04	0.06	0.43	0.00	0.56	6.1
	Gage 14	−0.25	0.82	−0.24	0.82	4.2
	Gage 13	0.05	0.14	0.05	0.13	2.6
Amite Comite River 2016-08-11–2016-08-17 (144 h)	Gage 07377500	73.43	305.49	236.86	539.36	2170
	Gage 07378000	—	—	—	—	—
	Gage 07377000	65.20	466.32	−185.73	616.66	3260
	Gage 07378500	69.63	653.39	−50.44	581.78	7700
	Gage 07380120	−47.56	373.88	−78.70	363.92	5640
Falls Lake 2018-09-16–2018-09-19 (72 h)	Gage 02085000	147.205	147.531	147.175	147.507	90.0
	Gage 0208521324	110.426	113.602	110.310	113.535	250
	Gage 02085500	89.296	109.273	88.979	109.272	410
	Gage 0208524090	111.453	111.675	111.438	111.664	90
	Gage 02085070	73.718	83.323	73.744	83.521	390
	Gage 0208675010	87.334	87.487	87.326	87.481	70
	Gage 02086500	76.360	76.713	76.477	76.815	490
	Gage 0208524975	72.863	82.987	72.737	83.055	400
	Gage 02086624	71.161	82.913	71.352	83.339	490
	Gage 02086849	75.669	75.702	75.688	75.721	90

Abbreviations: BIAS, mean error; RMSE, root mean square error.

Table 1 compares the statistical comparisons between the modeled discharge outcomes and their corresponding observed data for CNS and CNT. The statistical goodness of fit and overall quality of the two models is compared using mean error (BIAS) and root mean square error (RMSE) using the following equations:

$$\text{BIAS} = \frac{1}{N}\sum_{i=1}^{N}(E(\theta) - \theta), \tag{63}$$

$$\text{RMSE} = \sqrt{\frac{1}{N}\sum_{i=1}^{N}(E(\theta) - \theta)^2}, \tag{64}$$

where $E(\theta)$ is the discharge from the model (CNS or CNT), θ is the observed discharge, and N is the number of available observed data.

Table 1 shows that the model quality indexes are excellent for the first two case studies, Lower Mississippi and Goodwin creek, as the calculated BIAS and RMSE values are small compared to the observed maximum discharge in the channels. The BIAS and RMSE are higher for the latter two case studies compared to their peak discharges. Both case studies focused on flashy events where the flood peaks were a few magnitudes higher than the regular discharge, and the event dictated a very fast rise of the peak discharge. Many of these high BIAS and RMSE values originated from phase error issues as the model calculated the peak discharge earlier or later than the observed peak discharge. However, comparing the results between the CNT and CNS, we see that both models have very similar BIAS and RMSE at most of the compared stations except for Gage 07377500 and Gage 07377000 of Amit-Comite River. In these two cases, the calculated mean error in the CNT model is much higher than those of the CNS model. Identifying the cause of the difference is an opportunity for future work.

5.4 | Computation time requirement for the model simulation

The time required for model simulation is an important parameter when choosing a model for real-time operational forecasting. Therefore, we documented the processor wall time for each simulation as shown in Table 2. The model codes were written in Fortran90 while the computer used to run these simulations is a common desktop machine with a Core i7 processor (2.66 GHz) and 16 GB of RAM. In our work, we used an open-source gFortran compiler under the integrated development environment "Code::Blocks." However, our tests revealed that the use of intel Fortran compiler can provide approximately three times faster computation for both the CNS and CNT methods.

As shown in Table 2, the CNS model is not as computationally efficient as the CNT model. Due to the formulation of the CNS model, the model computational time step (Δt) is dependent on the Courant number criterion (also known as Courant–Friedrichs–Lewy/CFL condition). For this reason, test cases with small Δx required longer simulation periods for the CNS method. We applied a maximum courant number of 0.8 for the CNS simulations. The CNT model, however, is not dependent on the courant criterion as the discretization is strictly implicit on fixed temporal resolution. Thus, we used fixed $\Delta t = 600$ s for all the CNT model simulations.

5.5 | Characteristics of the outcome: Flood peak, flood duration, low-flow condition

Despite differences in their formulation, the results from the examples presented here indicate that the two diffusive wave models are similar in terms of their ability to capture flow dynamics. Both models showed a good prediction of flood peaks and flood durations.

TABLE 2 Comparison of simulation time requirements between the models.

				CNS		CNT	
Test case	Simulation period (days)	Total computational nodes	Spatial node to node distance, Δx(m)	Simulation time (s)	Δt (s)	Simulation time (s)	Δt (s)
Single channel	1	21	1000	0.31	500–615	0.05	600
Y-channel	1	37	1000	0.83	600–900	0.14	600
Mississippi	365	97	183–27,700	882.67	65–250	67.86	600
Goodwin	23	35	129–1487	57.69	36.3–207	4.81	600
Amite-Comite	12	237	13–19,280	430.67	6.9–23.4	9.91	600
Falls Lake	30	2292	20–3000	18,968.11	5–50	382.03	600

According to Moussa and Bocquillon (1995), the CNS and CNT models are efficient and may provide the exact solution at large wavelengths. The test result of the Mississippi river model (shown in Figure 7) confirms the statement. In the test case of the Y-channel network, the CNT model showed oscillation when the discharge hydrograph started to increase. This is an inherent characteristic of the model algorithm and may become prominent during low-flow conditions. The error due to the oscillation may increase at conditions with small celerity and large diffusivity (Moussa & Bocquillon, 1996b). The oscillation disappears at long waves and faster celerity; for example, no oscillation is seen in the Mississippi River test case since it has longer wavelengths. The Goodwin Creek test case also did not show any oscillation as it had faster wave celerity. A higher-order scheme instead of the CN could be examined in future applications (e.g., Dubey, 2013). However, the potential increase in computational burden should be carefully considered.

5.6 | Advantages and limitations of the diffusive wave approach for operational model applications

The NWM channel dataset provides cross-sectional data over 2.7 million locations over the CONUS. However, the cross-section spacings are highly variable. The spacings vary from a few meters (~4–6 m) to several kilometers (~10^3 m). Such large variations in the spacing create challenges for the higher-end routing approaches, namely the dynamic and diffusive models (Meselhe et al., 1997, 2021). However, the diffusive wave CNT option can robustly accommodate large variations in the spatial spacing without requiring a change in the time steps, as the model equation is discretized over the equal time spacing. This flexibility comes as a trade-off since the boundary condition of the model is required at the two extreme ends of the time continuum. On the other hand, the CNS diffusive wave is discretized over the unequal cross-sectional spacing and works best if the ratio between two immediate Δx's (shown as α in Equation 9) is ~<2. At a higher value of α, the calculated second derivative may introduce an error in the solution.

Operational models need to balance accuracy, speed, and robustness. The dynamic wave routing is the most accurate and has broad applicability to nearly all hydraulic conditions. However, it is also the most prone to numerical instability and the most computationally expensive. Thus, it is reserved for complex conditions that simpler approaches cannot resolve. The kinematic wave approach is the most computationally efficient and robust. The current MC of the NWM, for example, produces good results for fairly steep channels where backwater effects are less significant as it cannot produce any backwater effects, nor does it capture reverse flows. The diffusive wave approach is a reasonable compromise and can be applied to a large spectrum of hydraulic conditions. The approach can produce good results at low-gradient channels with backwater effects and resolve reverse directional flow. The CNT option is robust and computationally efficient. However, there are some limitations to the diffusive wave. The underlying simplification in the diffusive wave equation neglects the inertia term from the momentum conservation equation. Thus, the diffusive wave may not be accurate for a rapidly rising flood wave or other situations where the inertia term may become significant (Cappelaere, 1997). The pressure gradient significantly affects the flow propagation process, and its importance increases with lower channel slopes and steeper hydrographs (Morel-Seytoux et al., 1993). This condition also makes the stage variable important in the flood propagation calculation and contributes greatly to the calculations of celerity and diffusivity.

It should also be noted that the mass balance in the diffusive wave approach is only guaranteed when the celerity and the diffusively stay as a linear function of discharge only. According to Cappelaere (1997), when the ratio of celerity and diffusivity are constant for any discharge, the mass balance error is negligible. This criterion is applied in all diffusive waves analytical solutions as they assume celerity and the diffusivity as constant (e.g., Hayami's solution, Hayami, 1951). In practical applications, however, such as the NWM, this ratio changes throughout the flood peak and recession periods and changes spatially throughout a network. In general, steep channels have a higher C/D ratio than mild-slope channels. The applied limits on the celerity and the diffusivity assist in ensuring the stability of the model results. Furthermore, maintaining a bounded limit on the ratio of C/D throughout the channel network helps in minimizing the mass balance error in the model results.

As demonstrated here, both CNS and CNT models can be applied to high gradient channels. However, the potential benefit is limited, given that currently used MC model can also perform well in those channels and may impose less computational burden. For this reason, the future operational plan of the NWM follows a hybrid scheme, following suggestions made by Meselhe et al. (2021). The plan applies kinematic wave model (MC model) at high gradient channels and higher-order models (diffusive wave) at low-gradient channels with prominent backwater. The switching between the schemes will be based on calculated values of different dimensionless parameters.

6 | CONCLUSIONS

We present two diffusive wave models named CNS and CNT. Both models employ a finite-difference, implicit CN numerical solution with second-order accuracy. The CNS model employs finite differencing in space, while the CNT model employs finite differencing in time. We tested these two different solution methods using a variety of case studies covering a broad set of hydraulic conditions. The results from both models compared favorably with water level and discharge field observations.

The employed models' quality was also tested and compared with the MC model, which is currently used as the primary channel routing scheme for the NWM. The comparison revealed that the new models provide comparable discharge hydrographs to the MC method for regions with steep slopes and no backwater effects. For areas with small slopes where backwater effects are more prominent, the diffusive wave methods produce water level hydrographs comparable to field observations. In these low-gradient regions, the MC method produce unrealistically large water depths. The test cases presented here used geometry data available in the NWM database. In some cases, the channel cross-sections in the database severely underestimate the floodplain width. Tests revealed that the flood plain width underestimation impacts the routed flow quality for both diffusive models. However, the MC method, as it relies in simple normal depth calculations, is not affected by the quality of the channel geometry. This independence is advantageous for regions with steep slopes where the water depth is adequately captured by the uniform flow assumption, but it leads to significant errors in the water depth calculations in low-gradient regions where the water depth significantly deviates from the normal depth. Conversely, the diffusive wave models are directly affected by the quality of the channel geometry. When the channel and floodplain capacities are properly captured, they produce accurate flow and water depth hydrographs even in low-gradient regions with significant backwater effects. Thus, as the quality of the channel geometry improves in the NHD, the NWM would benefit from employing a diffusive wave model to produce reliable hydrographs in regions with flat terrain.

The results presented here also show that the CNS model is subject to a CFL criterion, limiting the computational time requirement as inversely proportional to the minimum spacing length of the domain. This limitation is costly for operational models. The second approach, the CNT model, uses a constant (and large) time stepping and is not limited by a CFL criterion. Thus, while both models provided comparable results with reasonable accuracy for most case studies, the CNT model shows higher computational efficiency, robustness, and ease of capturing spatially distributed lateral flows. These features make the CNT a suitable fit for operational forecast models. Model applications could benefit further from application of high-performance computing and parallel computing, both of which are currently being tested to become added model features in the near future.

AUTHOR CONTRIBUTIONS

Md Nazmul Azim Beg: Conceptualization; data curation; formal analysis; investigation; methodology; software; validation; visualization; writing – original draft; writing – review and editing. **Ehab A. Meselhe:** Conceptualization; formal analysis; funding acquisition; investigation; methodology; project administration; software; supervision; writing – original draft; writing – review and editing. **Dong Ha Kim:** Data curation; investigation; methodology; resources; software; writing – review and editing. **James Halgren:** Conceptualization; investigation; methodology; software; writing – review and editing. **Adam Wlostowski:** Investigation; methodology; resources; software. **Fred L. Ogden:** Investigation; methodology; resources; supervision; writing – review and editing. **Trey Flowers:** Project administration; resources; writing – review and editing.

ACKNOWLEDGMENTS

This research effort is performed in collaboration with the National Water Center and funded by the NOAA—Joint Technology Transfer Initiative (JJTI) under contract no.: NA18OAR4590394. The authors would like to acknowledge the collaboration with the National Water Center (NWC) in Tuscaloosa, AL.

CONFLICT OF INTEREST

The authors declare no conflict of interest.

DATA AVAILABILITY STATEMENT

To the extent permitted by data providers, all datasets and output results are posted on Zenodo at https://doi.org/10.5281/zenodo.6385057 and model formulations are available on https://github.com/MESH-Team/MESH_Code_irregular/releases/tag/Mesh_Diffusive_CNS_v0.1 and https://github.com/MESH-Team/MESH_CNT/releases/tag/MESH_CNT_v0.1.

ORCID


Md Nazmul Azim Beg https://orcid.org/0000-0002-7801-4272

REFERENCES

Alfieri, L., P. Burek, E. Dutra, B. Krzeminski, D. Muraro, J. Thielen, and F. Pappenberger. 2013. "GloFAS—Global Ensemble Streamflow Forecasting and Flood Early Warning." *Hydrology and Earth System Sciences* 17: 1161–75.

Barthélémy, S., S. Ricci, T. Morel, N. Goutal, E. Le Pape, and F. Zaoui. 2018. "On Operational Flood Forecasting System Involving 1D/2D Coupled Hydraulic Model and Data Assimilation." *Journal of Hydrology* 562: 623–34.

Beg, M.N.A., J. Leandro, P. Bhola, I. Konnerth, W. Willems, R.F. Carvalho, and M. Disse. 2019. "Discharge Interval Method for Uncertain Flood Forecasts Using a Flood Model Chain: City of Kulmbach." *Journal of Hydroinformatics* 21: 925–44.

Brunner, G.W., and J. Garbrecht. 1991. "A Muskingum-Cunge Channel Flow Routing Method for Drainage Networks." *ASCE Journal of Hydraulics* 117: 629–42.

Cappelaere, B. 1997. "Accurate Diffusive Wave Routing." *Journal of Hydraulic Engineering* 123: 174–81.
Carsell, K.M., N.D. Pingel, and D.T. Ford. 2004. "Quantifying the Benefit of a Flood Warning System." *Natural Hazards Review* 5: 131–40.
Cholet, C., J.B. Charlier, R. Moussa, M. Steinmann, and S. Denimal. 2017. "Assessing Lateral Flows and Solute Transport during Floods in a Conduit-Flow-Dominated Karst System Using the Inverse Problem for the Advection–Diffusion Equation." *Hydrology and Earth System Sciences* 21: 3635–53.
Chow, V.T., D.R. Maidment, and L.W. Mays. 1988. *Applied Hydrlogy* (B.J. Clark and J. Morris, eds.). Singapore: McGraw-Hill Book Company.
Cloke, H.L., and F. Pappenberger. 2009. "Ensemble Flood Forecasting: A Review." *Journal of Hydrology* 375: 613–26.
Cosgrove, B.A., E.P. Clark, A.L. Dugger, T. Flowers, D. Gochis, T.M. Graziano, and F.L. Ogden. 2021. "Operational Hydrologic Modeling: Current Status of NOAA's National Water Model and Plans for the Future." AGU Conference 2021, New Orleans. https://agu.confex.com/agu/fm21/meetingapp.cgi/Paper/895129.
Cunge, J.A. 1969. "On the Subject of A Flood Propagation Computation Method (Musklngum Method)." *Journal of Hydraulic Research* 7: 205–30.
De Saint-Venant, B. 1871. "Thorie Du Mouvement Non Permanent Des Eaux, Avec Application Aux Crues Des Rivires et l'Introduction Des Marés." *Compets Rendus de l'Academie Des Science de Paris* 73: 147–54.
Dewberry Engineers Inc. 2019. "Amite River Basin Numerical Model Project Report: 304."
Downer, C.W., and F.L. Ogden. 2004. "Appropriate Vertical Discretization of Richards' Equation for Two-Dimensional Watershed-Scale Modelling." *Hydrological Processes* 18: 1–22.
Dubey, R.K. 2013. "Total Variation Stability and Second-Order Accuracy at Extrema." *Electronic Journal of Differential Equations* 20: 53–63.
Fan, P., and J.C. Li. 2006. "Diffusive Wave Solutions for Open Channel Flows with Uniform and Concentrated Lateral Inflow." *Advances in Water Resources* 29: 1000–19.
Ferrick, M.G. 1985. *Analysis of River Wave Types*. New Hampshire: Hanver.
Ferrick, M.G. 2005. "Simple Wave and Monoclinal Wave Models: River Flow Surge Applications and Implications." *Water Resources Research* 41: 1–19.
Ferrick, M.G., J. Bilmes, and S.E. Long. 1984. "Modeling Rapidly Varied Flow in Tailwaters." *Water Resources Research* 20: 271–89.
Ferrick, M.G., J. Blimes, and S.E. Long. 1983. *Analysis of a Diffusion Wave Flow Routing Model with Application to Flow in Tailwaters*. New Hampshire: Hanver.
Gochis, D.J., M. Barlage, A. Dugger, K. Fitzgerald, L. Karsten, M. Mcallister, J. Mccreight, et al. 2018. "WRF-Hydro V5 Technical Description: The NCAR WRF-Hydro Modeling System Technical Description." https://ral.ucar.edu/sites/default/files/public/WRFHydroV5TechnicalDescription.pdf.
Hayami, S. 1951. "On the Propagation of Flood Waves." Disaster Prevention Research Institute, Kyoto University. https://books.google.com/books?id=nF-sOgAACAAJ.
Leandro, J., A. Gander, M.N.A. Beg, P. Bhola, I. Konnerth, W. Willems, R. Carvalho, and M. Disse. 2019. "Forecasting Upper and Lower Uncertainty Bands of River Flood Discharges with High Predictive Skill." *Journal of Hydrology* 576: 749–63.
Litrico, X., J.B. Pomet, and V. Guinot. 2010. "Simplified Nonlinear Modeling of River Flow Routing." *Advances in Water Resources* 33: 1015–23.
Madsen, H., and C. Skotner. 2005. "Adaptive State Updating in Real-Time River Flow Forecasting—A Combined Filtering and Error Forecasting Procedure." *Journal of Hydrology* 308: 302–12.
Meselhe, E., M.A. Lamjiri, K. Flint, S. Matus, E.D. White, and K. Mandli. 2021. "Continental Scale Heterogeneous Channel Flow Routing Strategy for Operational Forecasting Models." *Journal of the American Water Resources Association* 57: 209–21.
Meselhe, E.A., E.H. Habib, O.C. Oche, and S. Gautam. 2009. "Sensitivity of Conceptual and Physically Based Hydrologic Models to Temporal and Spatial Rainfall Sampling." *Journal of Hydrologic Engineering* 14: 711–20.
Meselhe, E.A., F. Sotiropoulos, and F.M. Holly. 1997. "Numerical Simulation of Transcritical Flow in Open Channels." *Journal of Hydraulic Engineering* 123: 774–83.
Mockus, V. 1967. "Chapter 17: Flood Routing." In *National Engineering Handbook*, edited by L. King, 1–68. Fort Worth, TX: National Geospatial Center of Excellence.
Morel-Seytoux, H.J., H. Fahmy, and J.-P. Lamagat. 1993. "A Composite Hydraulic and Statistical Flow-routing Method." *Water Resources Research* 29: 413–18.
Moussa, R. 1996. "Analytical Hayami Solution for the Diffusive Wave Flood Routing Problem with Lateral Inflow." *Hydrological Processes* 10: 1209–27.
Moussa, R., and C. Bocquillon. 1995. "A New Crank–Nicholson Algorithm For Solving The Diffusive Wave Flood Routing Equation Along A Complex Channel Network." *Transactions on Modelling and Simulation* 12: 11–21.
Moussa, R., and C. Bocquillon. 1996a. "Criteria for the Choice of Flood-Routing Methods in Natural Channels." *Journal of Hydrology* 186: 1–30.
Moussa, R., and C. Bocquillon. 1996b. "Algorithms for Solving the Diffusive Wave Flood Routing Equation." *Hydrological Processes* 10: 105–23.
Ogden, F.L., and P.Y. Julien. 1993. "Runoff Sensitivity to Temporal and Spatial Rainfall Variability at Runoff Plane and Small Basin Scales." *Water Resources Research* 29: 2589–97.
Sabur, M.A., and P.M. Steffler. 1996. "A Conservative Diffusion Wave Flood Routing Scheme for Channel Networks." *Canadian Journal of Civil Engineering* 23: 566–70.
Smith, A.A. 1980. "A Generalized Approach to Kinematic Flood Routing." *Journal of Hydrology* 45: 71–89.
Sriwongsitanon, N., J.E. Ball, and I. Cordery. 1998. "An Investigation of the Relationship between the Flood Wave Speed and Parameters in Runoff-Routing Models." *Hydrological Sciences Journal* 43: 197–213.
van der Wiel, K., S.B. Kapnick, G.J. van Oldenborgh, K. Whan, S. Philip, G.A. Vecchi, R.K. Singh, J. Arrighi, and H. Cullen. 2017. "Rapid Attribution of the August 2016 Flood-Inducing Extreme Precipitation in South Louisiana to Climate Change." *Hydrology and Earth System Sciences* 21: 897–921.
Wang, L., J.Q. Wu, W.J. Elliot, F.R. Fiedler, and S. Lapin. 2014. "Linear Diffusion-Wave Channel Routing Using a Discrete Hayami Convolution Method." *Journal of Hydrology* 509: 282–94.

How to cite this article: Beg, Md Nazmul Azim, Ehab A. Meselhe, Dong Ha Kim, James Halgren, Adam Wlostowski, Fred L. Ogden and Trey Flowers. 2023. "Diffusive wave models for operational forecasting of channel routing at continental scale." *Journal of the American Water Resources Association* 59(2): 257–280. https://doi.org/10.1111/1752-1688.13080.